Plasmonic Nanostructure on a Tapered Fiber for Chemical Detection

By

Joshua Ottorino Trevisanutto

A thesis submitted to the Faculty of Graduate Studies
Lakehead University
In partial fulfillment of the requirements for the degree of
Master of Science in
Physics

Department of Physics
Lakehead University
September 2017

Abstract

A simple, cost effective technique to manufacture plasmonic nanostructures as a Surface Enhanced Raman Spectroscopy (SERS) substrate was investigated. The plasmonic structure of gold nanorods was developed on the surface of a tapered fiber using the optical tweezing process from a colloidal solution. A unique grating like distribution of gold nanorods (GNRs) was formed. The effect of different laser wavelengths (632, 1064, and 1522 nm) on the assembly of the nanostructure was also investigated. The experiments were repeated with Gold nanospheres, which are referred to as gold nanoparticles (GNPs). However, no significant distribution of nanoparticles was observed. The tapered fiber was developed using dynamic and static chemical etching methods; a single-mode fiber (SMF 28), and a multimode fiber were used. The gold nanorods formed a grating like structure when optically tweezed using tapered multi-mode fiber. The potential use of the tapered fiber probe with nanostructure for application in SERS was investigated.

Contributions

Publications

Joshua O. Trevisanutto, Apichart Linhananta and G. Das,“ Plasmonic structure: fiber grating formed by gold nanorods on a tapered fiber", Optics Letters, vol. 41, no. 24, pp. 5789-5792, Dec. 15, 2016.

Joshua O. Trevisanutto and G. Das, “Fabrication of a Tapered Optical Fiber with Nanostructure Produced by Optical Tweezing”, Applications of Lasers for Sensing and Free Space Communications, OSA Laser Congress, Boston, USA, Oct. 30 to Nov. 4, 2016. (Proceedings)

Conferences

Joshua O. Trevisanutto and G. Das, “Plasmonic nanostructure for the detection of chemicals”, CAP Conference, Queen's University, Kingston, 27 May - 2 June, 2017.

Joshua O. Trevisanutto, Chetna Sharma and G. Das, “Development of a tapered fiber probe”, CAP Conference, University of Ottawa, Ottawa, 12-17 June, 2016.

Acknowledgements

Thank you to my supervisor Dr. Gautam Das, who gave me the opportunity to work with the Photonics Research Group, as well as provided me with both the basis of this project and the materials necessary to pursue it. His constant support and motivation made this possible.

Thank you to the Lakehead University Physics Department for motivating me to pursue graduate studies here, with a special thanks to my committee members Dr. Apichart Linhananta (co-supervisor), Dr. Mark Gallagher and Dr. Alla Reznik.

I would also like to thank all past and present members of the Photonics Research Group who have helped to develop this project and others over the years. I would especially like to thank Dr. Jonas Valiunas for both proof reading my thesis, as well as providing advice and guidance when working with fiber optics throughout my time here.

Additionally, I would like to thank Dr. Aicheng Chen for providing the support of his research group, particularly Dr. Sapanbir Thind, when working with Hydrofluoric acid to ensure everything was done safely. I would also like to thank Dr. Alla Reznik and her research group member Mr. Oleksii Semeniuk for giving us access to the Reinshaw Raman system in order to test our nanoprobe.

Dedicated to

My mother, Sandra Trevisanutto, for providing support at home and making my years of study here at Lakehead University possible.

Contents

List of Figures

List of Tables

Chapter 1

Introduction

1.1 Optical Fiber

Optical fiber is a cylindrical dielectric medium used to guide light. In its simplest form optical fibers are made up of two main components, the core and the cladding (Figure 1.1), where the core of the fiber has a slightly larger refractive index than the cladding. The difference in refractive indices between the core and cladding gives optical fiber its ability to guide light via total internal reflection. Additionally, the fiber is typically surrounded by a protective layer**,** which improves the fibers overall durability**.** Optical fiber can be divided into two main categories; (a) Step-index and (b) Graded-index, based on the refractive index distribution of the core with respect to the core radius. A fiber is referred to as step index if there is an abrupt decrease in the refractive index going from the core to the cladding. A gradient index fiber has a core refractive index which changes based on the radial distance from the center of the fiber [1]. Optical fiber can be manufactured from a variety of materials (e.g., silica, plastic and chalcogenide glass), but silica (SiO_2) is most commonly used [1]. In order to increase the index

of refraction of the core, oxides of metals (e.g., Al_2O_3) and semiconductors (e.g., GeO_2) are used [1].

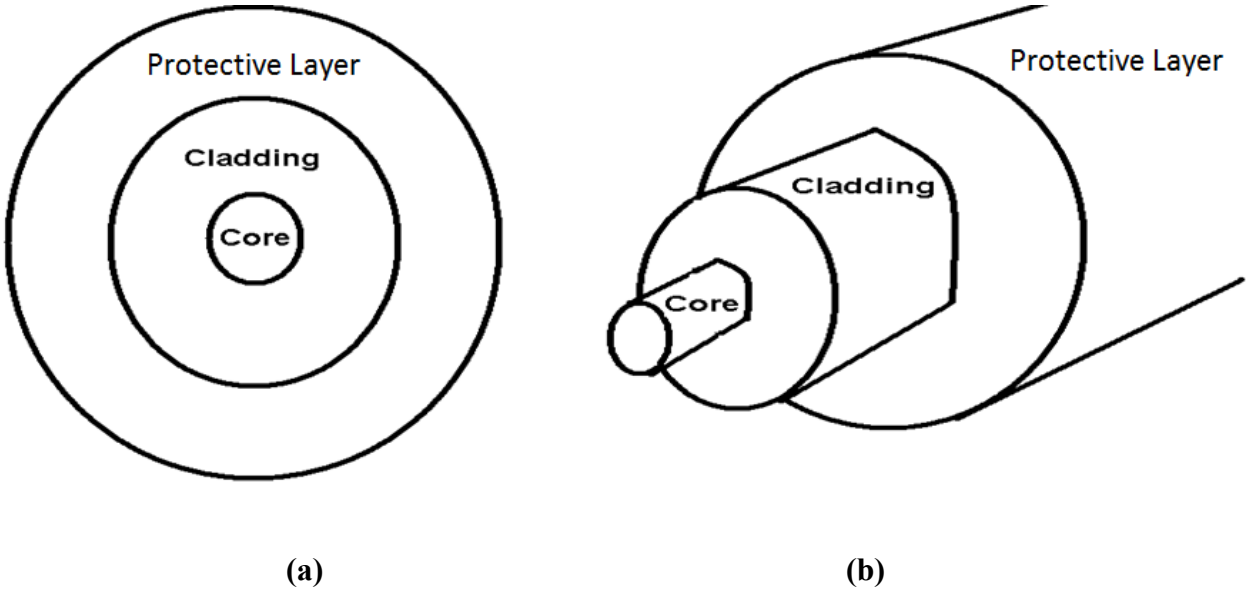

Figure 1.1 Structure of an optical fiber. (a) Cross sectional view of the fiber, (b) exploded view of each component.

Further, an optical fiber can be divided into two categories based on the number of transverse modes supported by the fiber. A transverse mode is defined as the distribution of the electric field inside the fiber [2]**.** A single mode fiber (SMF) can support only a single transverse mode, whereas multimode fiber (MMF) can support multiple transverse modes. In terms of the physical structure, the MMF has a much larger core diameter. Figure 1.2 shows a ray optics depiction of mode propagation in SMF and MMF optical fibers [1]. Generally, SMF is used for light transmission in optical communication when the transmission of light is required to occur over a long distance. A MMF is used for light transmission over a short distance [3]. A MMF

supports a large number of modes. In a SMF distortion of light signal is less compared to that in MMF[3].

The V number of an optical fiber determines the number of modes supported by the fiber. It is proportional to the radius and numerical aperture of the fiber, and inversely proportional to the wavelength of light propagating through the fiber, as given below [1]:

$$V = \frac{2\pi a}{\lambda}\sqrt{n_1^2 - n_2^2} \tag{1.1}$$

where a is the core radius, λ is the laser wavelength, n_1 is the core index of refraction, n_2 is the cladding index of refraction. As mentioned previously, the main physical distinction between SMF and MMF is MMF's larger core size. It is evident from **Equation 1.1** as the core radius increases the number of modes supported by the fiber also increases. The cut-off condition for single mode operation is V = 2.405, where a V number below this value indicates single mode operation.

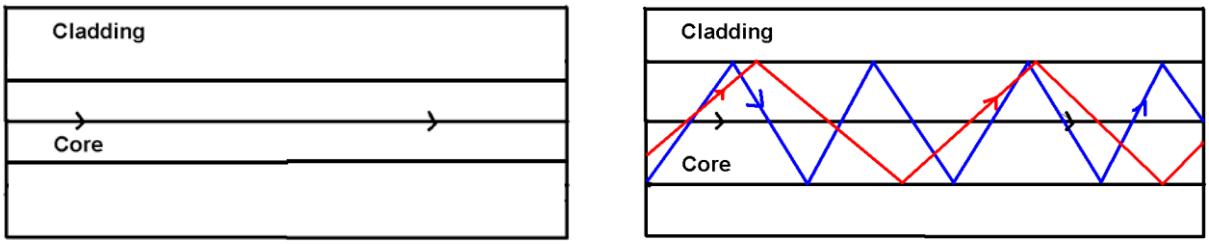

(a) (b)

Figure 1.2 A ray optics depiction of mode propagation in (a) SMF with a single (fundamental) mode, and (b) MMF with the fundamental mode as well as two higher order modes.

The light propagation inside the fiber is governed by the electromagnetic wave equation derived from Maxwell's equations as given below.

$$\nabla \times \boldsymbol{E} = -\mu \frac{\partial \boldsymbol{H}}{\partial t} \tag{1.2}$$

$$\nabla \times \mathbf{H} = -\varepsilon \frac{\partial \boldsymbol{E}}{\partial t} \tag{1.3}$$

$$\varepsilon \nabla \cdot \mathbf{E} = 0 \tag{1.4}$$

$$\mu \nabla \cdot \mathbf{H} = 0 \tag{1.5}$$

where ε is the permittivity, μ is the permeability, E is the electric field, H is the magnetic field, and t is time. The electromagnetic wave equations can be obtained by combining Maxwell's equations described above and given as [1]

$$\nabla^2 E = \varepsilon \mu \frac{\partial^2 E}{\partial t} \tag{1.6}$$

$$\nabla^2 H = \varepsilon\mu \frac{\partial^2 H}{\partial t} \tag{1.7}$$

The solution of the above equation in cylindrical coordinate for E and H fields can be expressed as:

$$\boldsymbol{E} = \boldsymbol{E_0}(r, \phi) e^{j(\omega t - \beta z)} \tag{1.8}$$

$$\boldsymbol{H} = \boldsymbol{H_0}(r, \phi) e^{j(\omega t - \beta z)} \tag{1.9}$$

where r, ϕ, and z are the cylindrical coordinates, β is the propagation constant and determined by solving the transcendental equation, which can be obtained by applying the boundary conditions at the core cladding interface, and ω is $2\pi v$ where v is the frequency of light. By substituting into Maxwell's equations and using a cylindrical coordinate system one can express the wave equations in cylindrical coordinates for H_z and E_z components as:

$$\frac{\partial^2 E_z}{\partial r^2} + \frac{1}{r}\frac{\partial E_z}{\partial r} + \frac{1}{r^2}\frac{\partial^2 E_z}{\partial \phi^2} + (\omega^2 \varepsilon\mu - \beta^2) E_z = 0 \tag{1.10}$$

$$\frac{\partial^2 H_z}{\partial r^2} + \frac{1}{r}\frac{\partial H_z}{\partial r} + \frac{1}{r^2}\frac{\partial^2 H_z}{\partial \phi^2} + (\omega^2 \varepsilon\mu - \beta^2) H_z = 0 \tag{1.11}$$

Using separation of variables methods E_z is can be expressed as:

$$E_z = \sigma A(r) B(\phi) C(z) D(t) \tag{1.12}$$

where σ is a constant, and it has already been assumed that *C(z) D(t)* has the form $e^{j(\omega t-\beta z)}$ as in **Equation 1.8** and **Equation 1.9**. Then, by making the observation that when ϕ changes by a total of 2π, E_z must not change, therefor:

$$B(\phi) = e^{jv\phi} \tag{1.13}$$

By combining both **Equation 1.13** as well as $e^{j(\omega t-\beta z)}$ with **Equation 1.12**, and then combining the result with **Equation 1.10** it is found that:

$$\sigma C(z)D(t)[\frac{\partial^2 A(r)}{\partial r^2}B(\phi) + \frac{1}{r}\frac{\partial A(r)}{\partial r}B(\phi) + \frac{1}{r^2}\frac{\partial^2 B(\phi)}{\partial \phi^2}A(r) + (\omega^2\varepsilon\mu - \beta^2)A(r)B(\phi)] = 0 \tag{1.14}$$

$$\frac{\partial^2 A(r)}{\partial r^2}B(\phi) + \frac{1}{r}\frac{\partial A(r)}{\partial r}B(\phi) + \frac{1}{r^2}(-v^2)A(r)B(\phi) + (\omega^2\varepsilon\mu - \beta^2)A(r)B(\phi) = 0 \tag{1.15}$$

$$\frac{\partial^2 A(r)}{\partial r^2} + \frac{1}{r}\frac{\partial A(r)}{\partial r} + \left(\omega^2\varepsilon\mu - \beta^2 - \frac{v^2}{r^2}\right)A(r) = 0 \tag{1.16}$$

where **Equation 1.16** resembles the Bessel differential equation. This expression can be derived by using H_z instead of E_z in an identical manner. In an optical fiber when $r = 0$ there must be a finite field, and when r goes to infinity the field must go to zero. The radial components of the fields can be expressed as [2]:

For r<a: $$J_v(ur) = A_1(r) \tag{1.17}$$

$$u^2 = \omega^2\varepsilon\mu - \beta^2 = (\frac{2\pi n_1}{\lambda})^2 - \beta^2 \tag{1.18}$$

For r>a: $$K_v(wr) = A_2(r) \tag{1.19}$$

$$w^2 = \omega^2\varepsilon\mu - \beta^2 = \beta^2 - (\frac{2\pi n_2}{\lambda})^2 \tag{1.20}$$

where $J_v(ur)$ is a Bessel function of the first kind, $K_v(wr)$ is a modified Bessel function of the second kind, v is the order of the Bessel function, a is the radius of the fiber core, n_1 is the refractive index of the core, and n_2 is the refractive index of the cladding. Because the boundary condition requires $K_v(wr)$ going to zero as r goes to infinity it follows that w must be positive, which means

$$\beta^2 > (\frac{2\pi n_2}{\lambda})^2 \tag{1.21}$$

Further, $J_v(ur)$ is given by the following equation:

$$J_v(ur) = \frac{1}{2\pi}\int_{-\pi}^{\pi} e^{jur\,sin(\theta) - jv\theta}\,d\theta \tag{1.22}$$

$J_v(ur)$ will be real if (ur) is real, which means u must be real since r is a radial distance. This implies that:

$$(\frac{2\pi n_1}{\lambda})^2 > \beta^2 \tag{1.23}$$

by combining **Equation 1.21** and **Equation 1.23** one will obtain the condition of wave propagation in optical fiber as:

$$\frac{2\pi n_1}{\lambda} \geq \beta \geq \frac{2\pi n_2}{\lambda} \tag{1.24}$$

By setting up a system of linear equations and taking the determinant it can be shown that β can be solved numerically by the following eigenvalue equation:

$$\left(\frac{J_\nu'(ur)}{uJ_\nu(ur)} + \frac{K_\nu'(wr)}{wK_\nu(wr)}\right)\left(\left(\frac{2\pi n_1}{\lambda}\right)^2 \frac{J_\nu'(ur)}{uJ_\nu(ur)} + \left(\frac{2\pi n_2}{\lambda}\right)^2 \frac{K_\nu'(wr)}{wK_\nu(wr)}\right) = \left(\frac{\beta\nu}{a}\right)^2 \left(\frac{1}{u^2} + \frac{1}{w^2}\right)^2 \tag{1.25}$$

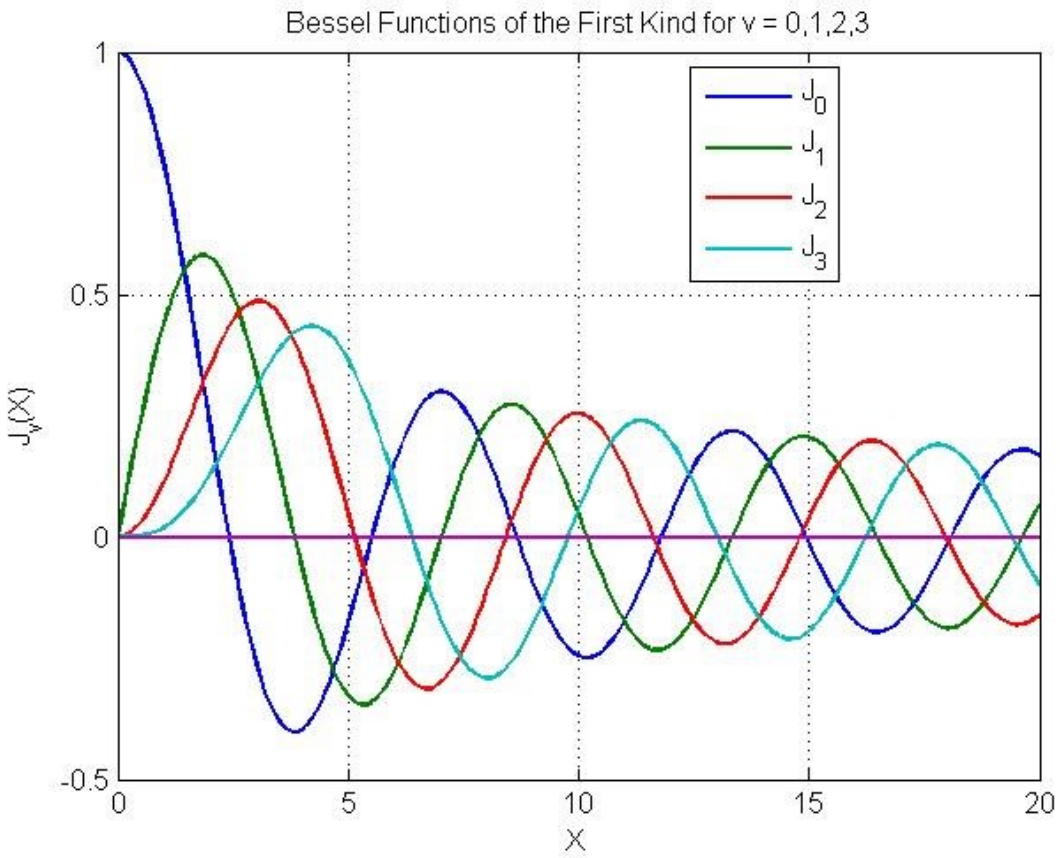

Figure 1.3 Bessel function of the first kind of order 0 to 3 where X is a variable

Each solution for β corresponds to a particular mode, where the index of the mode is determined by β_{vm}, where ν is the order of the Bessel function and m is the number of solutions for a particular value of ν. As can be seen in **Figure 1.3** the Bessel function has many solutions, when β is solved it has many zeros which appear in a similar way (within the boundaries set by **Equation 1.24**) [1].

When an exact analysis is used to calculate the number of modes supported in the fiber, they will generally fall into 4 categories; TE_{vm} (Transverse electric: electric field transverse to

the direction of propagation of the wave), TM_{vm} (Transverse magnetic: magnetic field transverse to the direction of propagation of the wave), as well as EH_{vm} and HE_{vm} (Hybrid modes). However, when the difference in the refractive indices of the core and cladding is much less than 1, the weakly guiding approximation is valid. In weakly guiding approximation the modes are known as "Linearly Polarized". These modes are represented as LP_{vm} (**Figure 1.4)**, and they can be expressed as a combination of exact modes. The LP_{0m} modes are made up of the HE_{1m} family, the LP_{1m} modes are made up of the TE_{0m}, TM_{0m}, and HE_{2m} mode family, and finally the remaining LP_{vm} (where $v>2$) modes are made up of the $HE_{v+1,m}$ and $EH_{v-1,m}$ mode family [1]**.**

The characteristic parameters of an optical fiber are the (a) Mode field distribution; (b) Mode field diameter; and (c) Dispersion. The knowledge of the mode field distribution can assist one to develop passive optical components, where the interaction of the evanescent field with its surroundings (e.g., Directional coupler) is very important. In order to obtain a large evanescent field, it is important to operate the fiber at low V-number [V=Normalized propagation constant], at which more of the power carried by the fiber will be in the cladding [4]. The mode field diameter is an estimate of the distribution of light in the propagating mode. Fiber dispersion determines how far a signal can be propagated coherently.

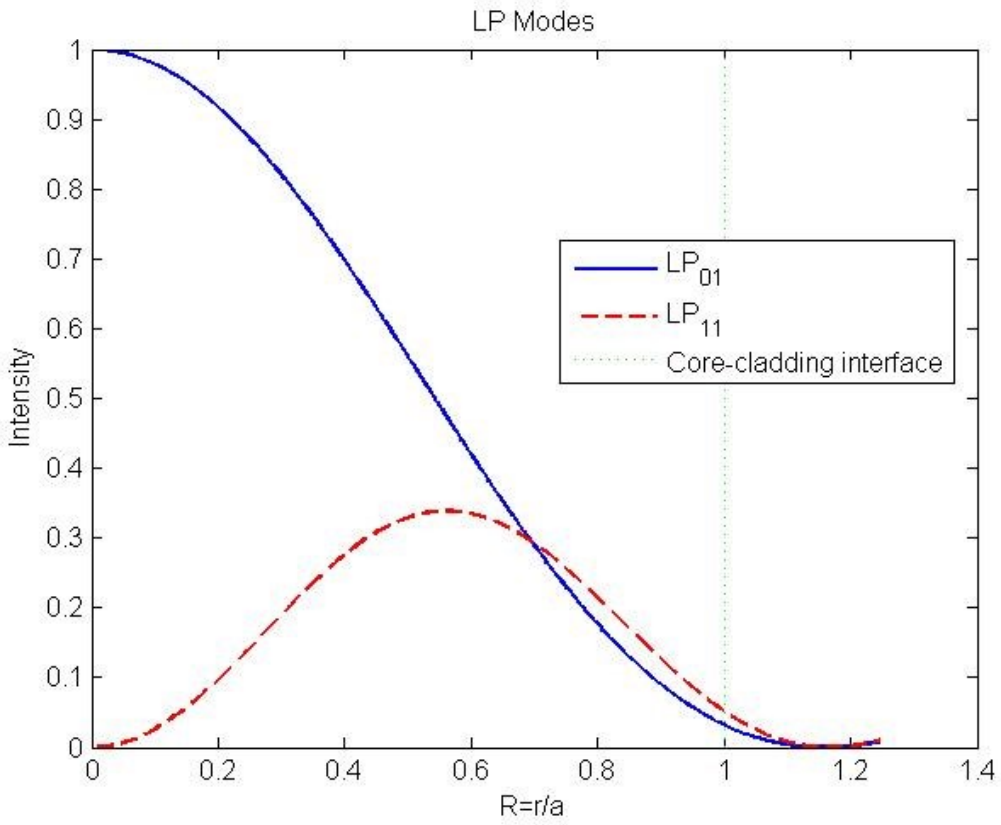

Figure 1.4 Normalized intensity of LP_{01} and LP_{11} modes for a fiber with V=6.5 [Equation 1.1], where n_2=1.4408, n_1 = 1.4578, R is the normalized radius (r/a)and 'a' is the fiber diameter which is 7.22 μm.

1.2 Tapered Optical Fiber

The properties of the optical fiber strongly depend on its geometric shape, for example: polarization maintaining fiber is constructed with an elliptical core [5], the V parameter which is dependent on core size (as described previously) determines the single mode and multi-mode operation of an optical fiber. A tapered shape fiber, which has a very strong evanescent field, is

another example of manipulating a fiber's physical characteristics in order to produce passive optical devices (**Figure 1.5)**. As described previously, a lower V parameter will result in more power coupled into the cladding of the fiber [4]. As the tapered fiber core decreases, the V parameter (**Equation 1.1**) will also decrease.

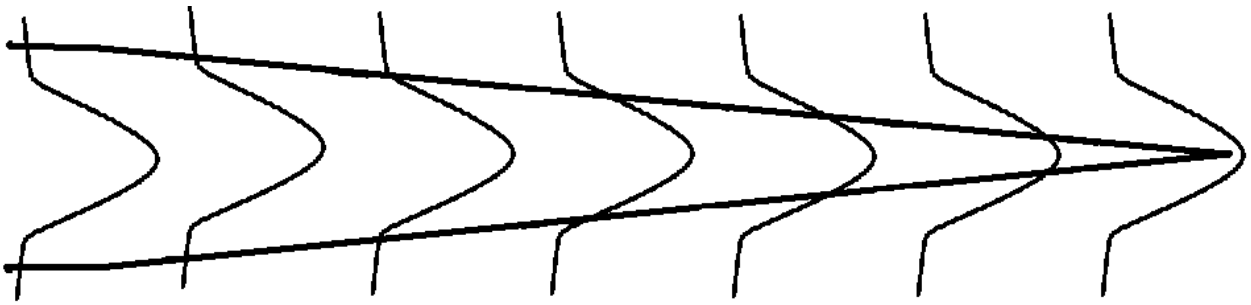

Figure 1.5 The core of a tapered fiber is exposed to the environment; the increase in the power coupled to the cladding is depicted as the fiber's core diameter decreases further down the length of the fiber.

Figure 1.6 shows the structure of a tapered optical fiber. Tapered fibers can be manufactured by heating-pulling, polishing, or chemically etching a regular fiber [6-8]. A tapered optical fiber has several differences when compared to an untapered fiber. In the tapered fiber the protective layer is no longer present at the end, leaving a portion of the cladding, as well as the tapered tip exposed to the environment. Additionally, at the point where the tapering begins, the cladding is etched away progressively until it is completely gone. The core is exposed to the environment once the cladding is completely etched, and it too is progressively etched down to a very small tip diameter. The manufacturing process of the tapered fibers will be discussed further in Chapter 2.

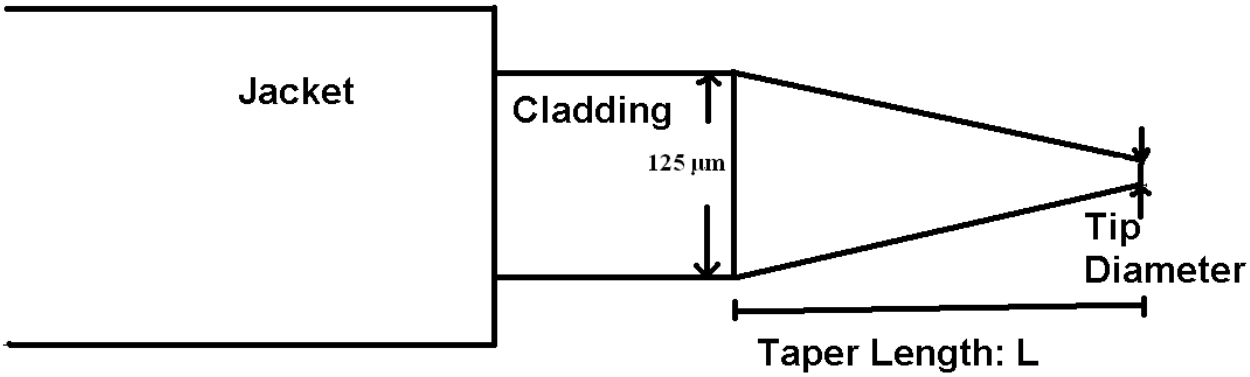

Figure 1.6 Schematic of a tapered fiber.

In this thesis the physical characteristics of tapered fiber were examined using a Scanning Electron Microscope (SEM). The tapered fibers were adhered to a double sided carbon tape on top of an SEM sample holder (**Figure 1.7)**. Due to the extremely small tip diameter of the tapered fiber, and without the protective layer adhering them to the tape, this was a delicate process. The most effective method to do this without breaking the tapered fiber required the tapered tip to be cut as short as possible. The freshly cleaved end of the tip was then pushed into the tape with tweezers, and then tipped over and gently pressed into the tape.

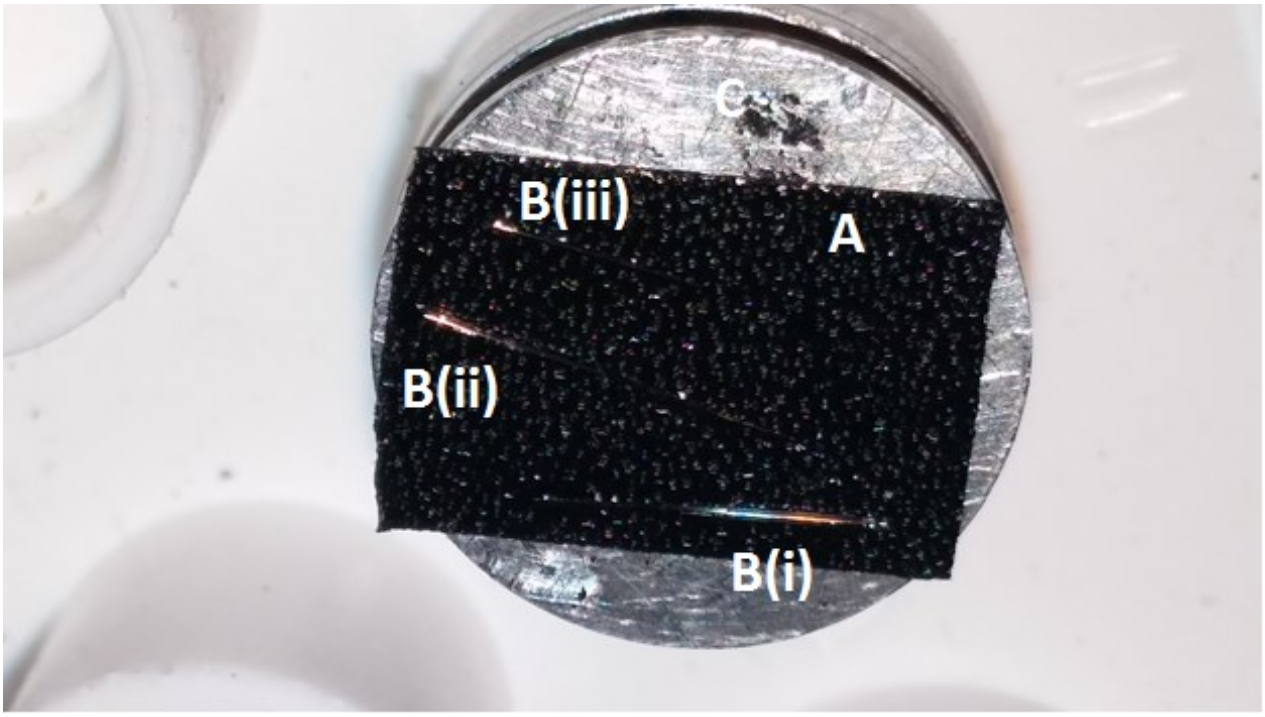

Figure 1.7 Tapered optical fiber (B(i,ii,iii)) adhered to carbon tape (A) on an SEM sample holder (C).

The important parameters for a tapered fiber are tapered length, tip diameter and cone angle. As shown in **Figure 1.6**, the tapered length is the measurement from where the fiber begins to taper, to the point of the fiber tip. The tip diameter is the diameter of the taper at the very end where the fiber has been completely etched away. The cone angle for a right circular cone is calculated by extrapolating the tapered fiber to a point (**Figure 1.8)** [9]. The equation which relates the cone angle to the taper length and tip diameter is derived as follows [where a 2D representation of a tapered fiber is used and is constructed by two linear equations].

$$y_1 = m_1 x_1 + b_1 \tag{1.27}$$

Equation 1.27 is used to represent the upper tapered fiber surface, where m_1 represents the slope, b_1 the y-intercept, and (x_1,y_1) is a point.

$$m_1 = \frac{r-R}{L-0} = \frac{r-R}{L} \tag{1.28}$$

where L is the taper length, r and R are radii of the tapered tip and fiber cladding, respectively. After substituting the point (L, r) into **Equation 1.27** and combining it with **Equation 1.28**:

$$r = \frac{r-R}{L}L + b_1 \tag{1.29}$$

$$b_1 = R \tag{1.30}$$

where, the value of b_1 from **Equation 1.30** is equal to R.

$$y_2 = m_2 x_2 + b_2 \tag{1.31}$$

Equation 1.31 represents the lower surface of the tapered fiber,

$$m_2 = \frac{-r-(-R)}{L-0} = -\frac{r-R}{L} \tag{1.32}$$

After substituting the point (L,-r) into **Equation 1.31** and combining it with **Equation 1.32** we obtained:

$$-r = -\frac{r-R}{L}L + b_2 \tag{1.33}$$

$$b_2 = -R \tag{1.34}$$

where the value of b_2 is -R. The fiber will have a total length of L+s **(Figure 1.8)**, where s is some positive number, when the tip is extrapolated to a point which is represented by the intersection of y_1 and y_2,

$$y_2 = y_1 \tag{1.35}$$

$$-\frac{r-R}{L}x - R = \frac{r-R}{L}x + R \tag{1.36}$$

$$x = \frac{RL}{R-r} \tag{1.37}$$

Therefore, the fiber will be extrapolated to a point at a length L+s = x = $\frac{RL}{R-r}$ (**Equation 1.37**). Now using basic trigonometry for a right angled triangle,

$$\tan(\phi) = \frac{R}{L+S} = \frac{R}{(\frac{RL}{R-r})} = \frac{R-r}{L} \tag{1.38}$$

$$\phi = \arctan(\frac{R-r}{L}) \tag{1.39}$$

and as the cone angle θ is represented by 2ϕ,

$$\theta = 2\phi = 2\arctan[\frac{R-r}{L}] \tag{1.40}$$

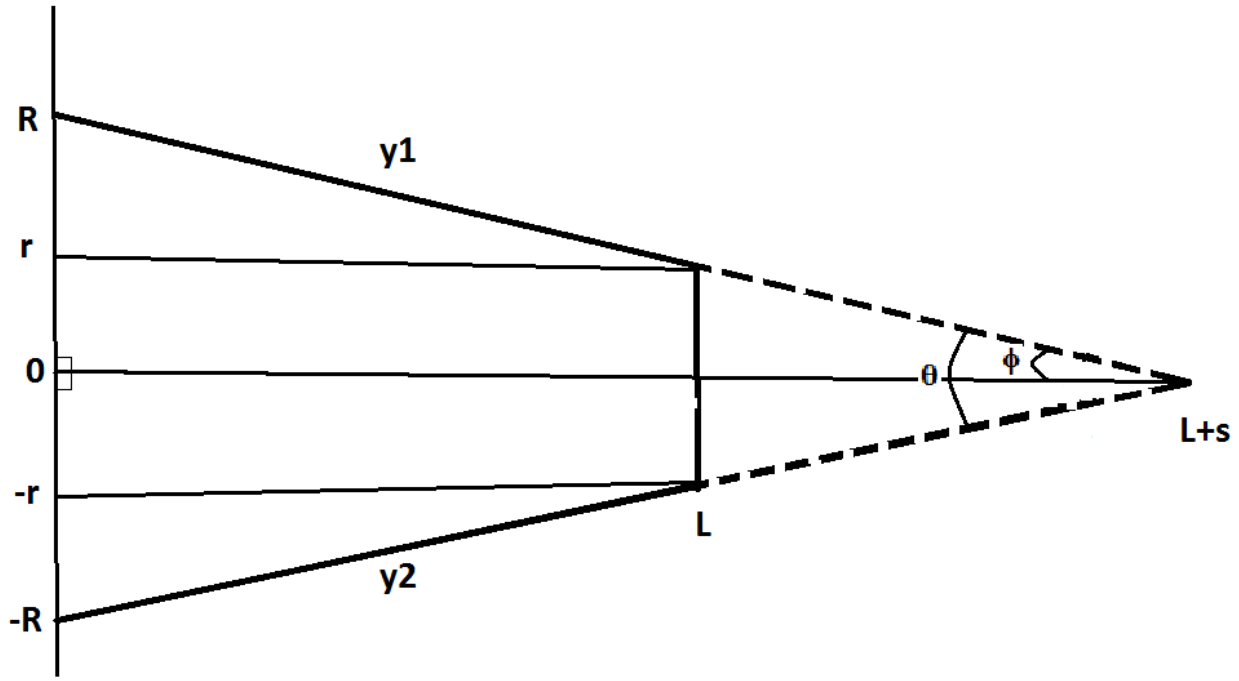

Figure 1.8 2D representation of a tapered fiber with cladding radius R, tip radius r, and taper length L extrapolated to a point L+s in order to calculate the cone angle θ, where ϕ is half of the cone angle. y_1 and y_2 are top and bottom surfaces of the tip respectively.

1.3 Nanoparticles and Nanorods

A metal object with a size on the order of nanometers (sub-wavelength dimensions) which is smaller than the electron mean free path provides unique optical properties [10]. More specifically, its particular size and shape become quite important and can influence its optical properties, which are different than those observed in bulk materials [10]. Metal objects on par with this particular size and spherical in shape are referred to as nanoparticles.

Noble metal nanoparticles in particular have attracted significant interest due to their catalytic properties [11] as well as their strong Localized Surface Plasmon Resonance (LSPR) [12]. Additionally, metallic nanoparticles possess unique plasmonic properties which have been utilized for spectroscopy [13], biosensors [14], and in cancer treatments [15]. Perhaps the most important parameter to consider about nanoparticles is the LSPR frequency. In Surface Plasmon Resonance (SPR) electrons in a bulk material oscillate at a frequency related to the density of the conduction electrons, and the frequency tends to be in the ultraviolet frequency range [16]. This oscillation can be induced by an electromagnetic wave in resonance with the plasmon frequency [16;17]. Both SPR and LSPR are oscillations of the negatively charged conduction band electrons with respect to the positively charged nucleus [16;18]**.** However, LSPR occurs when the conduction electrons are confined to a finite volume (such as a nanoparticle) where the particle size is smaller than the wavelength of the incident light; because of this the LSPR condition is greatly dependant on the particular volume and shape which confines the electrons [16;19]. The condition of the LSPR is satisfied when the frequency of the plasmon is approximately the same as the frequency of the incident electromagnetic wave [20]. The specific wavelength condition for which LSPR occurs is strongly dependant on the nanoparticle material, size, shape, and surrounding environment [19;21].

At the LSPR wavelength, the number of photons that are either released with a particular frequency (Scattered) or converted into phonons (absorbed) will be maximized [21;22]. Another consequence of the LSPR is a dramatically enhanced electric field in close proximity to the nanoparticles [23]. This enhanced field is the basis of surface enhanced Raman spectroscopy (SERS) [24;25]. The electric field around a gold nanoparticle with a radius much less than the

wavelength of light, after interaction with incident electromagnetic waves can be solved using Maxwell's equations and given as in **Equation 1.41** [24;25]

$$E_{out}(\mathrm{x},\mathrm{y},\mathrm{z}) = E_0\hat{z}\left[\frac{\varepsilon_{in}-\varepsilon_{out}}{\varepsilon_{in}+2\varepsilon_{out}}\right]a^3E_0\left[\frac{\hat{z}}{r^3}-\frac{3z}{r^5}(x\hat{x}+y\hat{y}+z\hat{z})\right] \quad (1.41)$$

where E_{out} is the electric field surrounding the particle, E_0 is the incident electric field, ε_{in} is the dielectric constant of the material, ε_{out} is the dielectric constant of the medium, a is the radius of the gold nanoparticle. In order for field enhancement to be maximised, the materials dielectric constant (which is wavelength dependant) should be approximately $-2\varepsilon_{out}$. For gold nanoparticles this condition tends to occur in the visible region of electromagnetic spectrum (as discussed in the following paragraph); a plot of the dielectric constant of gold nanoparticles versus wavelength can be found in reference [26]. In Raman spectroscopy, photons incident on a sample are scattered and detected. The majority of photons which interact with the sample will undergo Rayleigh scattering. However, a small portion will be inelastically scattered (Stokes shifted), resulting in a scattered photon with a different energy, and therefore a different wavelength (**Figure 1.9**). This wavelength shift is characteristic of the sample and can be used as a signature for identifying the sample [27]. In conventional Raman spectroscopy the number of inelastically scattered photons is extremely low [28]. However SERS dramatically increases the Raman signal with enhancement factors of 10^{10} or more [29]. The Stokes shifted radiation can be enhanced by the same mechanism behind the local incident field enhancement, which greatly increases the intensity of the SERS signal, which is discussed in detail in reference [30]. The Raman signal is proportional to E^4, where E is the electric field [31]. The signal enhancement factor (EF) for SERS is given by the following relation [24;25]

$$EF(w_v) = \frac{|E_{out}(w)^2||E_{out}(w-w_v)^2|}{E_0^4} = \frac{I_{SERS}(w_v)}{N_{surf}} \div \frac{I_{NRS}(w_v)}{N_{vol}} \quad (1.42)$$

where $E_{out}(w)$ is the enhanced electric field of the incident light, $E_{out}(w\text{-}w_v)$ is the enhanced electric field of the stokes shifted light, I_{SERS} is the intensity of the SERS signal, which is then divided by $N_{surf,}$ (the number of molecules on the SERS substrate surface experiencing field enhancement), I_{NRS} is intensity of the normal Raman signal, which is then divided by N_{vol} (the number of molecules in the volume excited by the incident radiation). This means that an enhanced electric field will give rise to a greatly enhanced Raman signal, which is the principle of SERS [32]. A number of researchers have demonstrated the benefits of SERS by utilizing nanoparticles excited at their LSPR frequency [33].

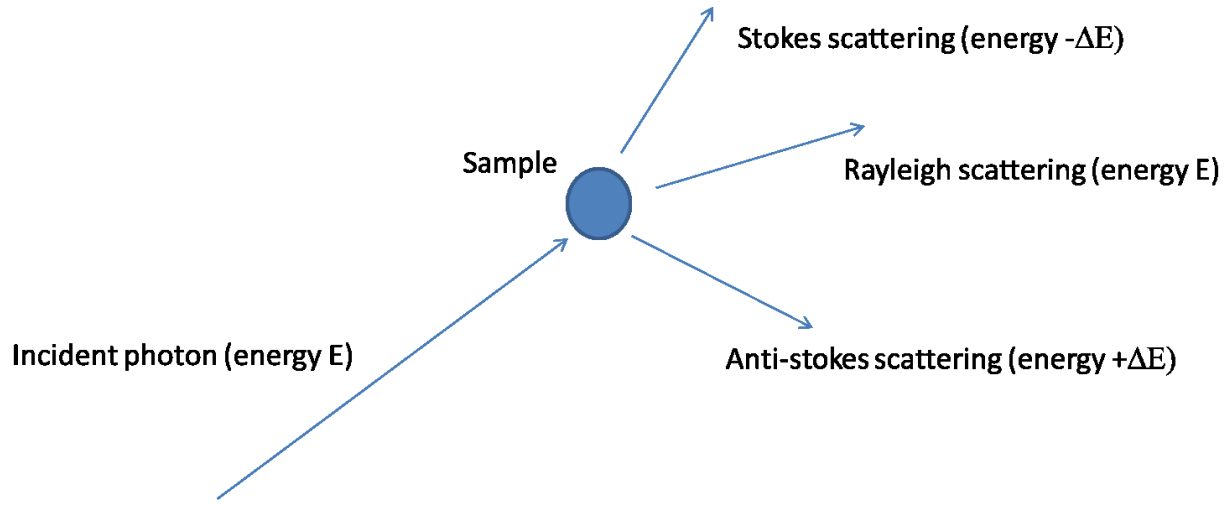

Figure 1.9 Interaction of an incident photon with an arbitrary sample resulting in three possible scattering scenarios: Stokes scattering, where a quanta of energy is lost from the photon, Anti-stokes scattering, where a quanta of energy is gained by the photon, and Rayleigh scattering, where no quanta of energy is gained or lost by the photon. The quanta of energy gained or lost (ΔE) is characteristic of the sample.

The simplest example of a metallic nanoparticle is the gold nanosphere (GNP). Due to its symmetry a nanosphere will have a single LSPR wavelength, which usually lies in the 520 nm wavelength range [34]. A number of theoretical investigations have been done to examine the electric field enhancement around GNPs when excited by a light source at the LSPR wavelength [35]. As the radius of the GNP is increased the resonance wavelength for LSPR tends to shift to a higher wavelength [21]. Another nanomaterial relevant to this thesis is the gold nanorod (GNR). GNRs are asymmetric, and have two LSPR wavelengths; a transverse resonance wavelength peak, as well as a longitudinal resonance wavelength peak. The longitudinal LSPR is the strongest of the two, and is caused by electron oscillations along the length, whereas the transverse LSPR is caused by electron oscillations along the diameter [36]. Further, theoretical

investigation has shown that the electric field is strongly enhanced around GNRs when excited by a light source corresponding to either the longitudinal or transverse LSPR wavelength [37]. The longitudinal LSPR peak location is highly dependent on the GNR aspect ratio (ratio of the length and diameter of the GNR), and as the aspect ratio is increased it shifts towards the infrared region of the electromagnetic spectrum [38]. Due to the GNR's longitudinal LSPR frequency dependence on aspect ratio, it can be tuned to a particular wavelength [39].

There are a number of different metallic nanoparticles of different shapes which have been studied, such as nano-triangles [40;41], nano-stars [41], and nano-shells around a silica core [42] among others. In this thesis, GNPs with an LSPR wavelength of 528 nm, and GNRs with a transverse LSPR of 508 nm and a longitudinal LSPR wavelength of 1064 nm were used (**Figure 1.10**).

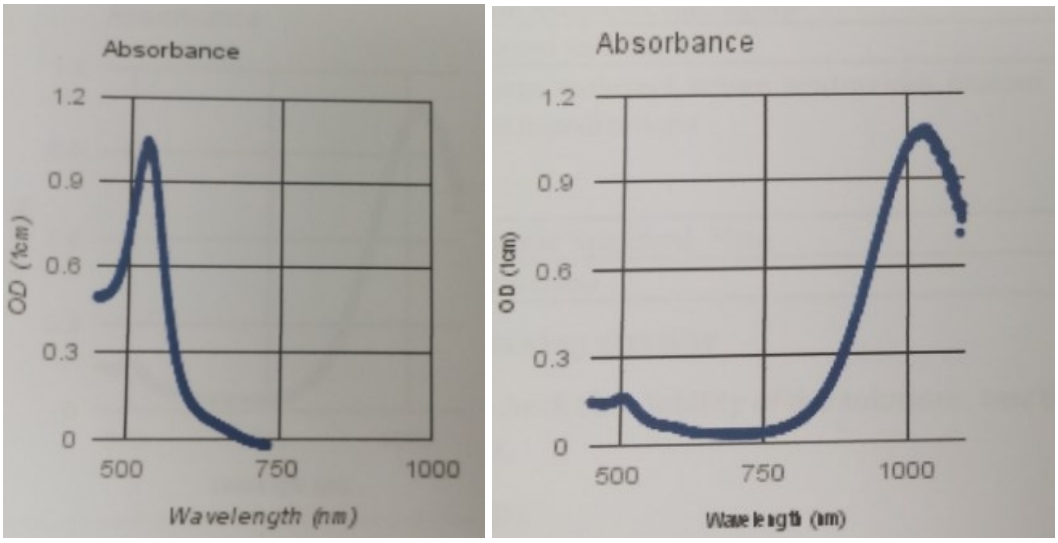

(a) (b)

Figure 1.10 Absorption spectrum provided by the manufacturer Nanopartz: (a) 40 nm diameter GNPs, and (b) 67 nm long and 10 nm diameter GNRs. Note: Peaks corresponds to their LSPR wavelengths.

1.4 Organization of the Thesis

Chapter 1 is a brief introduction on the subjects of this research which include: optical fiber and the wave equations which can be used to define the modes it can support, tapered fiber and how it differs from standard optical fiber and how it is characterized, the optical properties of metallic nanoparticles focusing on localized surface plasmon resonance (LSPR), and Raman spectroscopy. Chapter 2 describes the procedure used to manufacture the tapered optical fiber using both dynamic and static chemical etching processes, the results of this process are described. Chapter 3 describes the optical tweezing process used in order to obtain gold nanoparticle and gold nanorod deposition on the tapered fiber surface. The results are examined and compared between different laser wavelengths. Chapter 4 concludes the thesis, and describes the use of the tapered fiber as a potential chemical sensor, specifically for use as a surface enhanced Raman spectroscopy (SERS) probe.

1.5 Conclusions

Tapered optical fiber has several characteristics which separate it from regular optical fiber. The fiber can produce a strong evanescent field in the surrounding space, which can be utilized for a number of applications. The parameters which are used to characterize the properties of a tapered fiber include the taper length, tip diameter, and cone angle. Further, the cone angle is calculated by extrapolating the tip to a point assuming it is conical in shape.

Additionally, metallic nanoparticles (e.g., gold nanoparticle) of varying shapes and sizes have interesting optical properties such as LSPR. When metallic nanoparticles are excited by a laser source which meets their particular LSPR condition, the local electric field in close proximity to them is greatly enhanced.

Chapter 2

Design of a Tapered Fiber Nanoprobe

2.1 Introduction

There have been many applications which have taken advantage of tapered optical fiber, such as: sensing [43], nonlinear optics [44], optical trapping of micron or nanometer size particles both on the tip [45] and on the tapered fiber surface [46], passive optical devices [47], and in microscopy [48]. A number of techniques have been used to manufacture tapered fiber such as the heating and pulling method, where a carbon dioxide laser is used as the heat source, and a specialized pulling apparatus is used to draw out the fiber [6]. Another method to create tapered fiber involves polishing the fiber mechanically [7].

In this thesis a chemical etching process was used to make tapered optical fiber, which will be discussed in this chapter.

Tapered optical fiber manufactured by chemical etching can be done as a static or dynamic process [8]. In this research project both dynamic and static etching processes were used to make tapered fiber with a desired tapered size and tip diameter for potential application in SERS. In both processes 1.5 millilitres of hydrofluoric (HF) acid of 50% concentration was used. In order to prevent evaporation of the HF acid a protection layer of organic solvent (Isooctane) was used in both methods. This protection layer keeps the HF volume constant, as well as prevents the entire unsubmerged length of the fiber from etching by HF vapor [49;50]. For the dynamic etching process, the fiber is withdrawn from the etchant at a particular velocity in order to obtain the desired physical characteristics (e.g., taper length and tip diameter) of the tapered fiber [51]. As the fiber is withdrawn, the portion which exits the HF into the organic solvent is no longer etched, however the portion remaining in the HF solution is, which produces the tapered shape. For static etching the HF meniscus rises up along the surface of the fiber when it is inserted into the solution due to surface tension [8;52]. As the silica is etched away the interaction area with the fiber decreases, causing the meniscus to move further down the fiber, thus creating the characteristic tapered shape [8;52]. The characteristics of both static and dynamically etched tips will be covered in the following section.

In addition, the chemical etching process can also be used to manufacture optical microfiber, which is also an attractive tool to develop an optical sensor based on spectroscopy. In this process instead of creating a taper, it creates a section of fiber which has been uniformly etched, and rather than terminating, the microfiber continues until it has transformed back to the original fiber shape as shown in **Figure 2.1** [53].

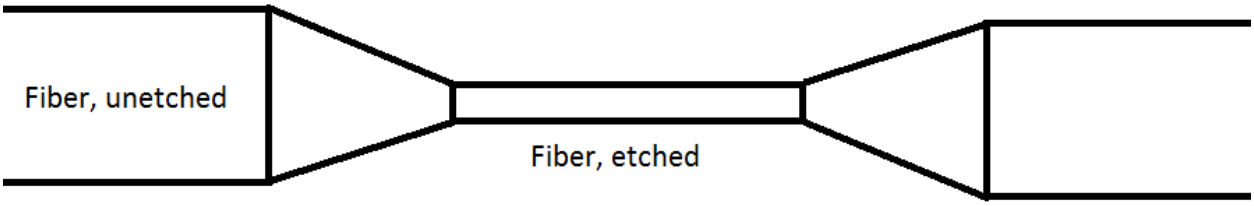

Figure 2.1 Diagram of optical microfiber.

2.2 Dynamically Etched Tapered Fiber

The tapered fiber was produced from a multimode fiber (Nufern: FUD-4309 MM-S106. 5/125-22FA). In order to control the position of the fiber during the etching process a computer controlled translation stage was used (ThorLabs TDC001). The translation stage was controlled by the ThorLabs APT interfacing software (Version 2.3.4701.37075), which allowed controlling the translation stage velocity, acceleration, and position. The APT application allows users to create, and import files from Microsoft Excel which can be utilized to control the movement of the translation stage. A vial was positioned below the fiber which contained both the etchant [1.5 ml of 50% HF acid], and a layer of organic solvent (isooctane) as shown in **Figure 2.2**.

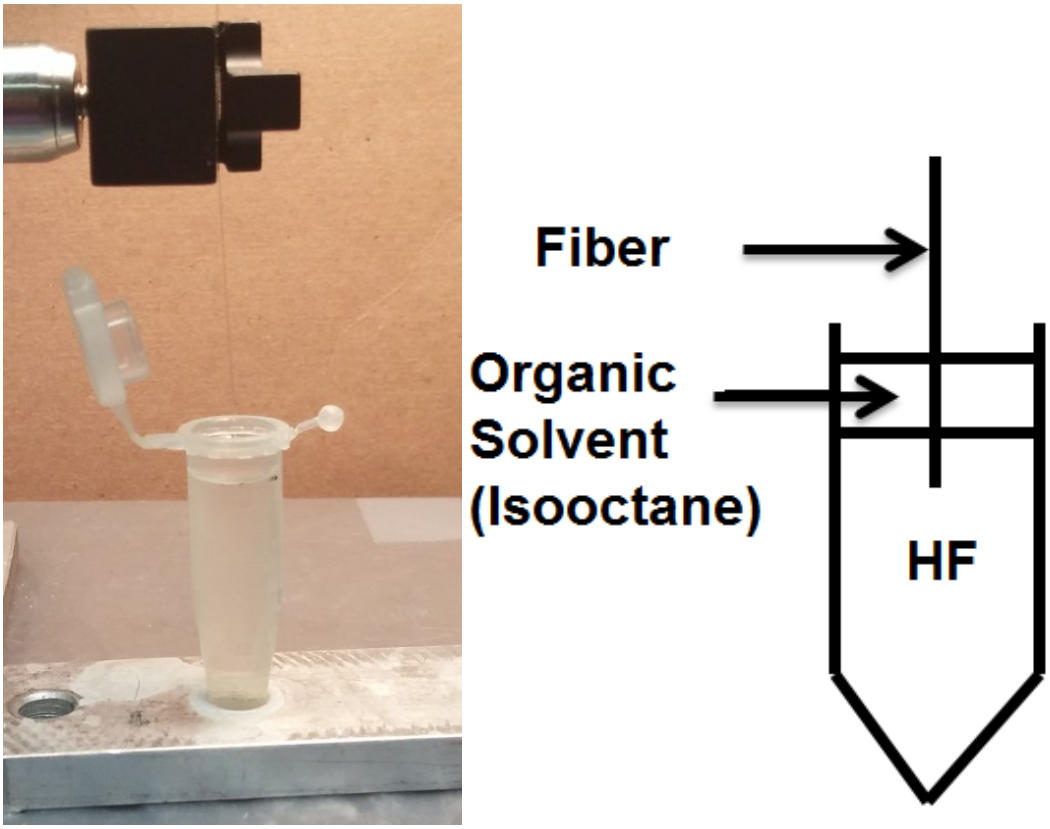

Figure 2.2 Experimental setup for tapering optical fiber.

The tip diameter (~ 100 nm) and tapered length (~ 2.0 mm) of the dynamically etched tapered fiber probe were achieved by controlling the speed of the translation stage as well as the penetration depth of the fiber into the HF. In order to achieve a consistent tip size on the order of 100 nm, the fiber was 'overshot' into the HF, which implies that more optical fiber was inserted into the HF at the beginning of the etching process than would be withdrawn. Doing this eliminated the need for an accurate measurement of the fibers initial position relative to the HF meniscus at the beginning of the etching process. This was due to the fact that the fiber was completely etched through before the entire inserted length was able to be withdrawn. Since the

fiber would be etched through before the full inserted length was withdrawn, the end of the etching process was dependant on the time required for HF to completely etch the fiber (**Figure 2.3**). Going from part C to part D in **Figure 2.3** shows how the HF completely etched through the diameter of the fiber, reducing its overall length compared to what was initially inserted and leaving what is left outside of the HF and in the protection layer of organic solvent. The total time required for the HF to completely etch through the 125 μm diameter MMF was ~ 39.5 minutes. If the total etching time and the desired taper length is known, the required withdrawal speed of the fiber can be calculated by using the linear displacement equation $d = vt$, where d is distance, v is velocity, and t is time. For a 2.0 mm taper length and at the known 39.5 min etching time, a fiber withdrawal velocity of 8.4×10^{-4} mm/s is required.

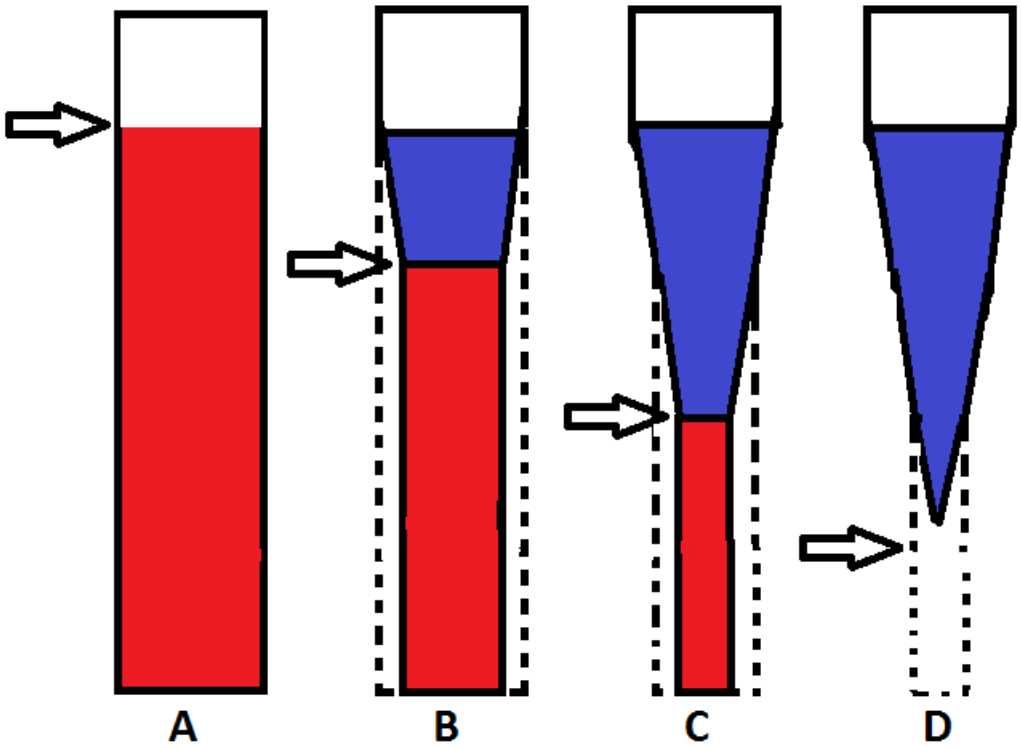

Figure 2.3 Red colour indicates that the fiber is immersed in the HF and is being etched, blue colour indicates that the fiber has exited the HF and is within the organic solvent layer or in the air above it. Dashed line indicates portion of fiber etched away from previous stage. Arrow indicates HF meniscus level; this height does not change, the fiber is actually in motion but the frame of reference has been shifted in each stage for ease of comparison. Figures A to D depict the etching process of the fiber as it is withdrawn from the HF solution.

The procedure for creating a dynamically etched fiber begins by removing the polymer protective layer and cleaving the fiber to make a flat end. The fiber is then attached to the translation stage; a rough measurement is taken of its initial position relative to the cap of the vial containing the HF. The distance between the cap of the vial and the HF meniscus was measured beforehand and remained relatively consistent (~ 8 mm) between experiments due to the organic solvent layer preventing evaporation. Furthermore, small changes in the meniscus

position were not an issue due to the fiber depth being 'overshot', as previously described. The measurements were entered into an Excel sheet which calculated the movement steps. The first two steps move the fiber to the position of the cap (which is now open and out of the way) and then to the HF meniscus. The third step 'overshot' the fiber into the HF (3.5 mm was inserted even though a 2 mm taper length was desired). The fourth step withdrew the fiber at the calculated withdrawal speed of 8.4×10^{-4} mm/s until it was no longer submerged in the HF. The final step brought the fiber, now tapered, back to its initial position (**Figure 2.4**). The tapered fiber produced using this method had an approximately 2 mm taper length, and an 80 nm tip diameter (**Figure 2.5**).

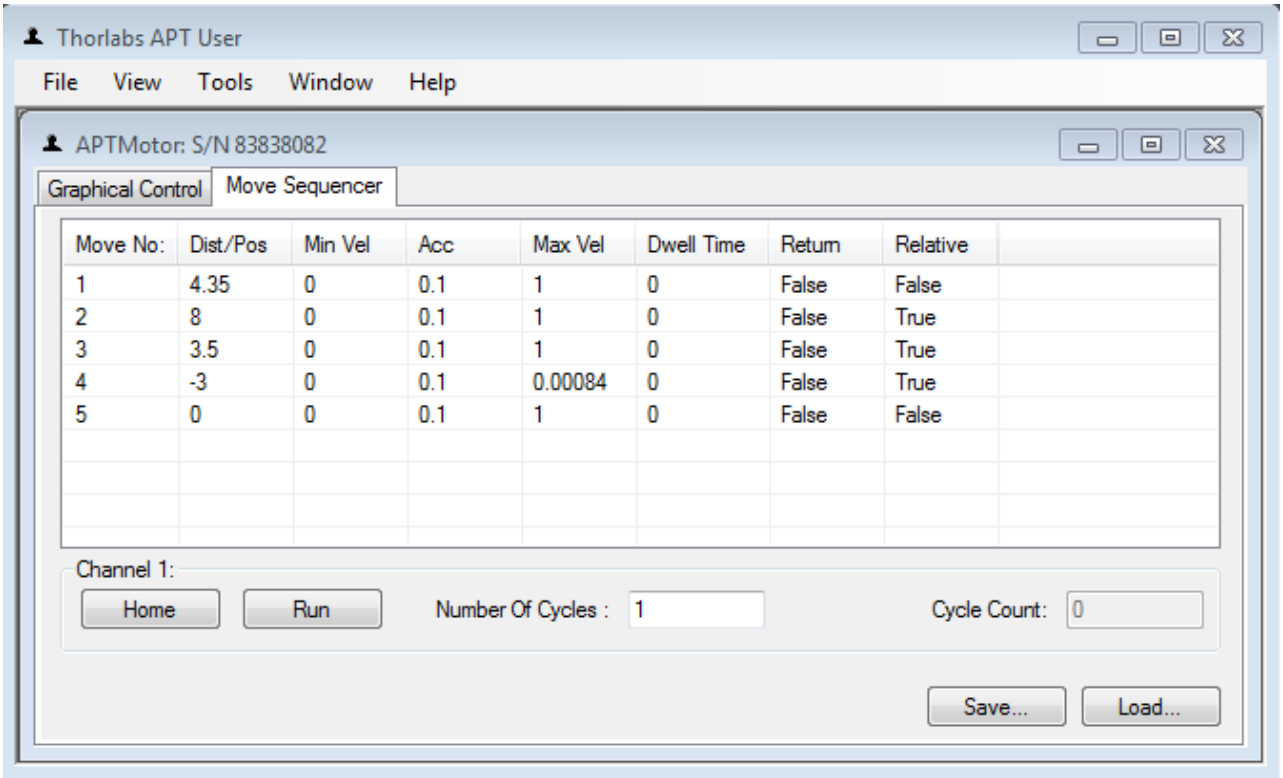

Figure 2.4 Sequence of moves executed to produce the tapered fiber. "Move No:" defines the step number to be executed. "Dist/Pos" is given in millimetres and defines the displacement of the fiber in the given step. "Min Vel" defines the minimum velocity of the fibers motion in mm/s. "Acc" defines the fibers acceleration in $mm/s^{2.}$ "Max Vel" defines the fibers maximum velocity in mm/s. "Dwell Time" defines how much delay there is between step executions in milliseconds. "Return" equal to True would return the fiber to the home position at the end of the step, "Return" equal to False does not. "Relative" equal to False defines the displacement given in "Dist/Pos" as being relative to the home position (Distance = 0), whereas "Relative" equal to True defines the displacement relative to the previous step.

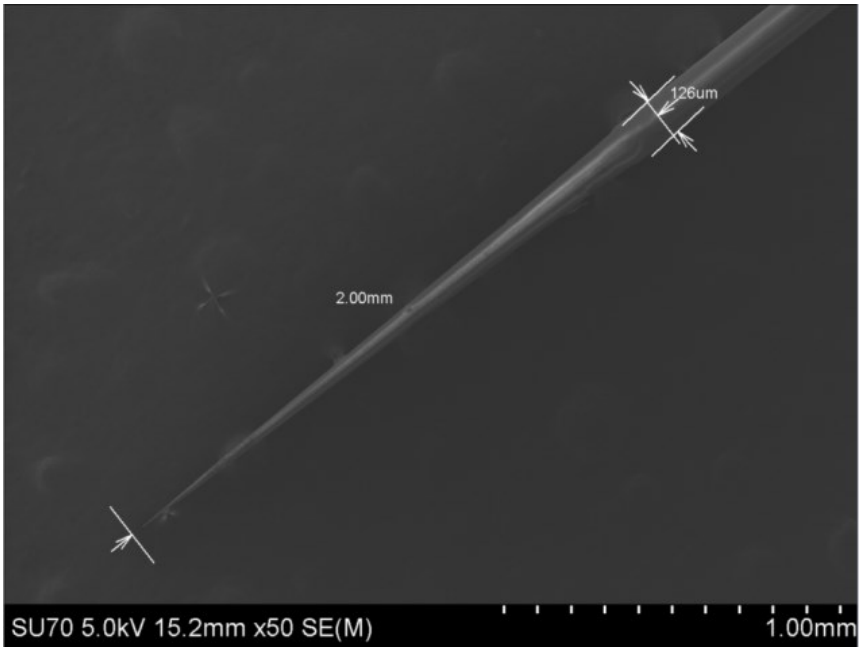

(a)

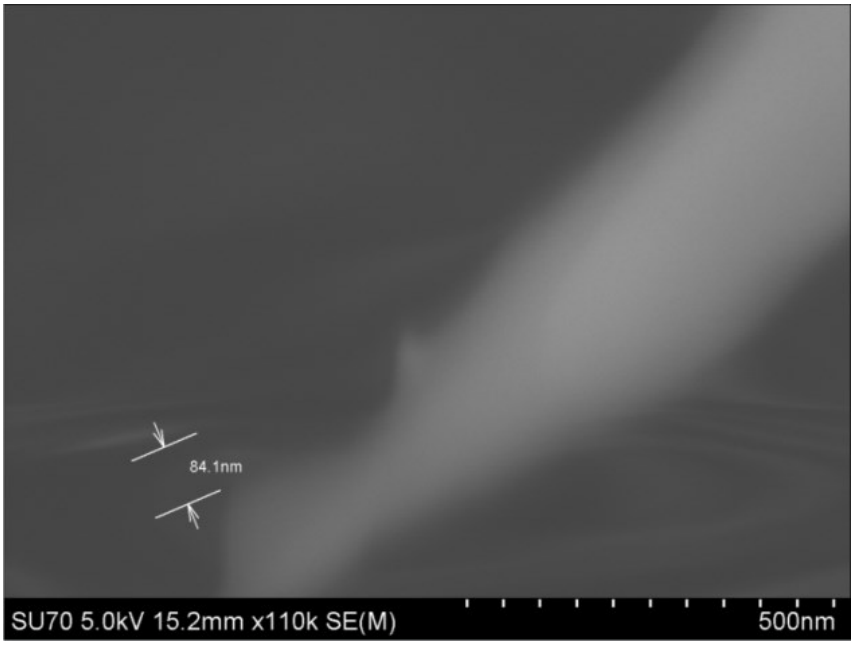

(b)

Figure 2.5 SEM image of the tapered fiber made using the dynamic etching process. The taper length was measured to be 2.00 mm, and the tip diameter was measured to be 84.1 nm. (a) Tapered fiber; and (b) the tip of the tapered fiber.

The tapered fibers used for the experiments in the following chapter were manufactured using the dynamic etching process with a pull speed of 0.00084 mm/s, however to demonstrate how the fiber characteristics could be altered two dynamically etched fibers were made at different pull speeds. The first was manufactured with a pull speed of 0.00072 mm/s. The tapered fiber had a taper length of 1.64 mm and tip diameter of 88 nm (**Figure 2.6**). As previously shown, when the pull speed of the fiber is multiplied by the time required to completely etch the fiber, the taper length is approximately calculated as: (0.00072 mm/s)*(39.5 min)*(60 s/min) = 1.71 mm, which is close to the experimental value. A second fiber was manufactured with a pull speed of 0.00063 mm/s. The tapered fiber had a taper length of 1.44 mm and a tip diameter of 308 nm (**Figure 2.7**). Though the tip diameter tended to be larger for this set of fibers (on the order of 300 nm) they were still made consistently. The calculated taper length was (0.00063 mm/s)*(39.5 min)*(60 s/min) = 1.49 mm, which was close to the experimental value. Hence, it was possible to control and predict the taper length of the fiber using simple calculations.

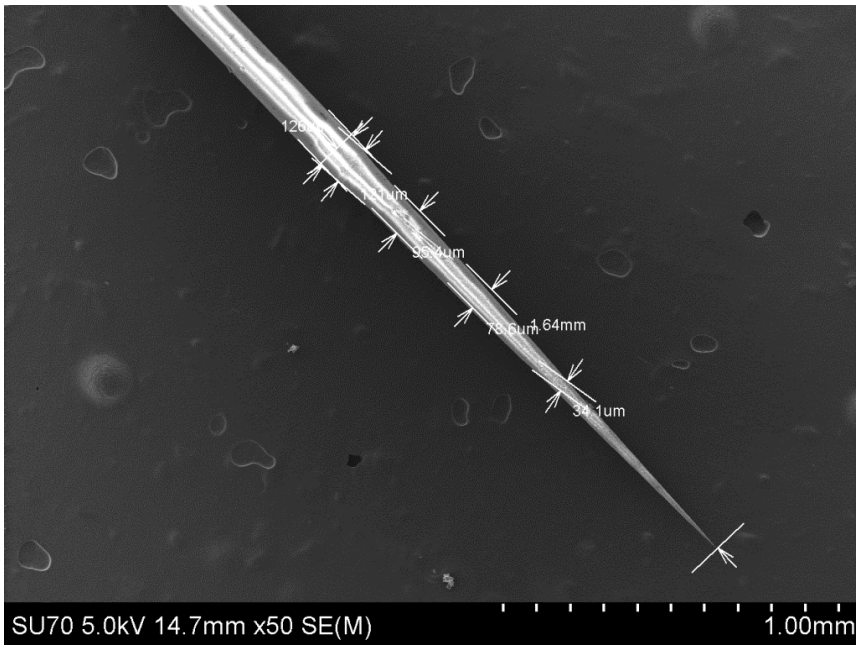

(a)

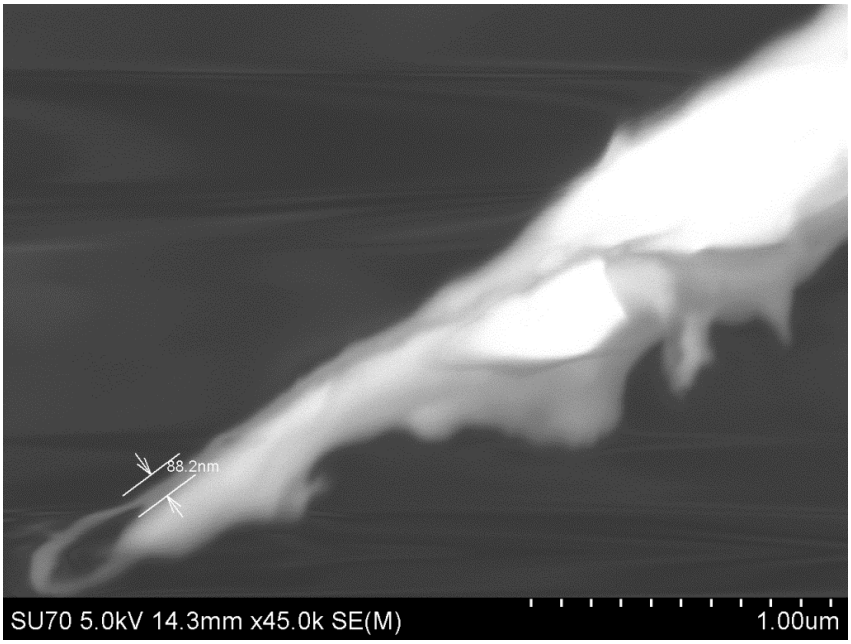

(b)

Figure 2.6 Tapered fiber made by the dynamic etching process (pull speed: 0. 00072 mm/s; taper length: 1.64 mm; and tip diameter 88 nm). (a) Tapered fiber, and (b) Tapered fiber tip.

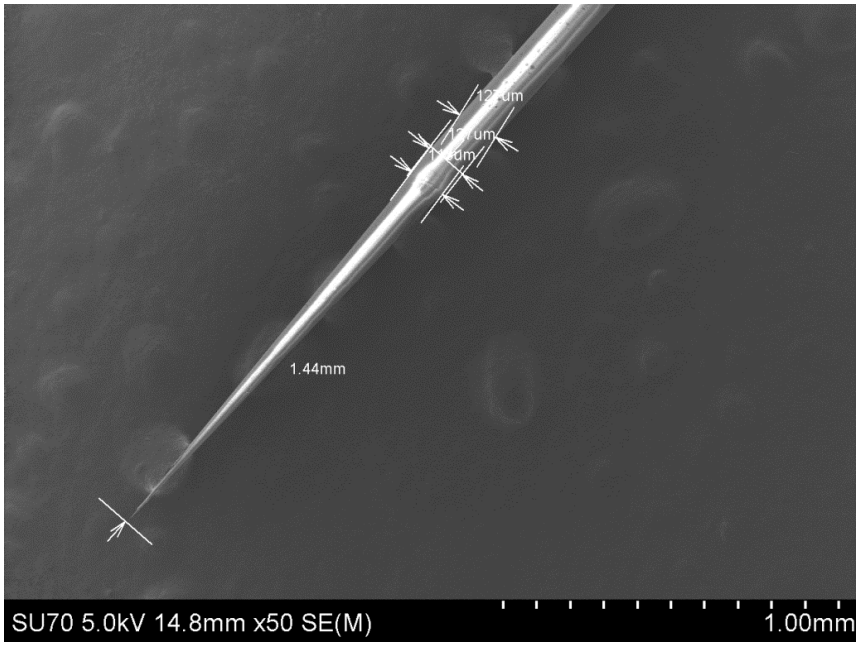

(a)

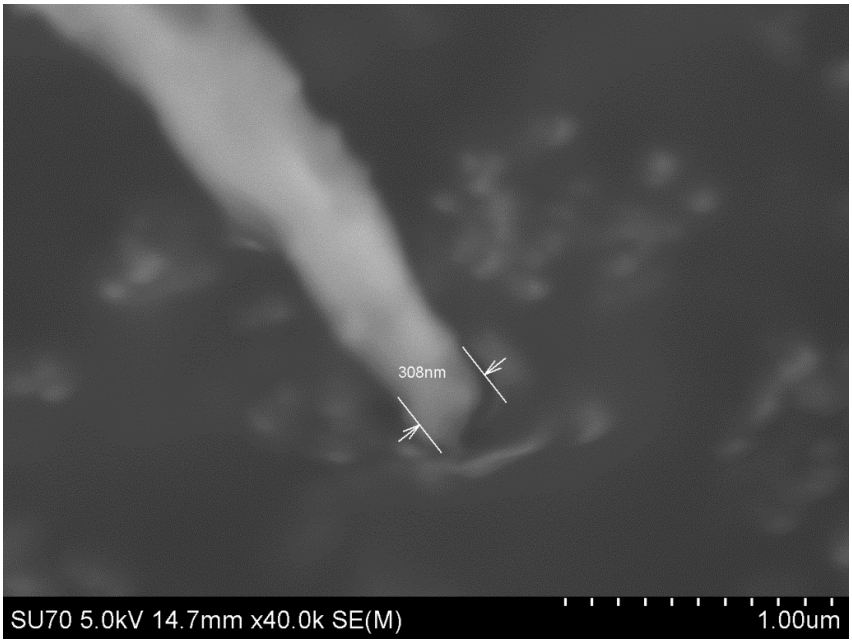

(b)

Figure 2.7 Tapered fiber made by the dynamic etching process (pull speed: 0.00063 mm/s; taper length: 1.44 mm; and tip diameter: 308 nm.) (a) Tapered fiber, and (b) Tapered fiber tip.

2.3 Statically Etched Tapered Fiber

The process for making the statically etched fiber is very similar to the dynamic etching process with the exception of the fourth step that was removed. For the static etching process the fiber is left statically submerged in the HF. After approximately 39.5 minutes the fiber is withdrawn to the starting position, and is observed to have been completely etched through by the HF (**Figure 2.8**). It is possible to alter the cone angle of a statically etched fiber by changing the organic solvent used as the protective layer. Since different organic solvents have varying characteristics, such as surface tension and density, the height of the HF meniscus on the fiber and the resulting etched tip can be changed [8;52], however in this thesis only isooctane was used. The fiber produced using this method had an approximately 0.25 mm taper length and 70 nm tip diameter (**Figure 2.9**).

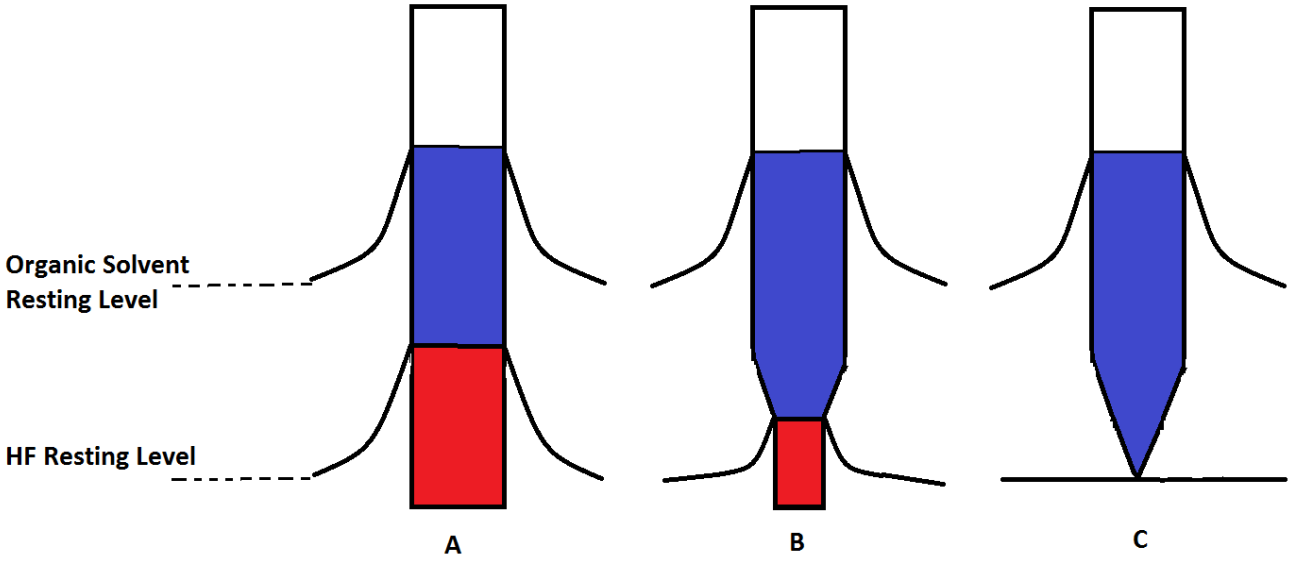

Figure 2.8 Red colour indicates that the fiber is immersed in the HF and is being etched, blue colour indicates that the fiber is within the organic solvent layer and is not being etched, white color indicates the fiber is in the air past the organic solvent layer. The static etching process proceeds from left to right where C is the final step where the etching process is complete and the entire fiber tip lies in the organic solvent, which occurs after 39.5 minutes with the specific fiber and HF concentration used.

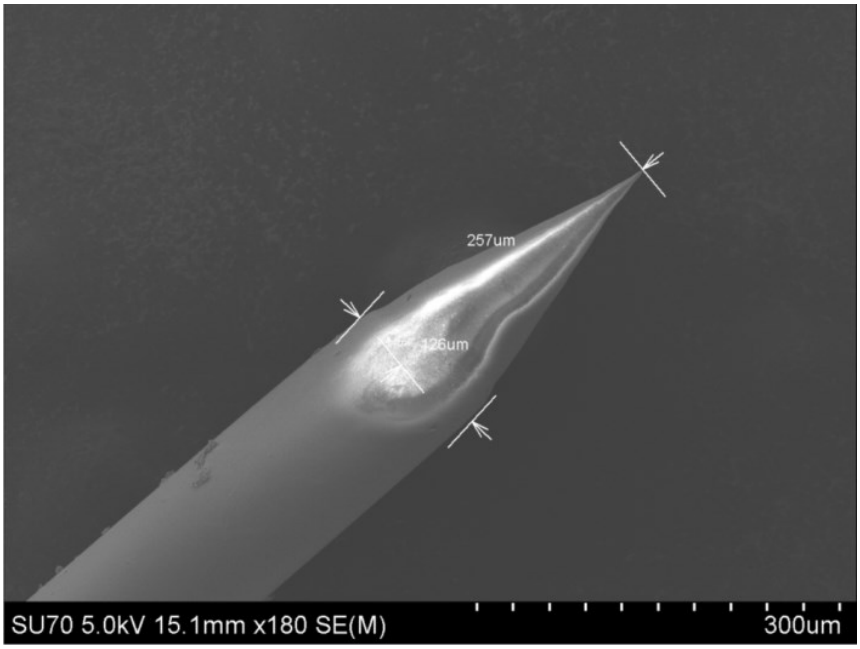

(a)

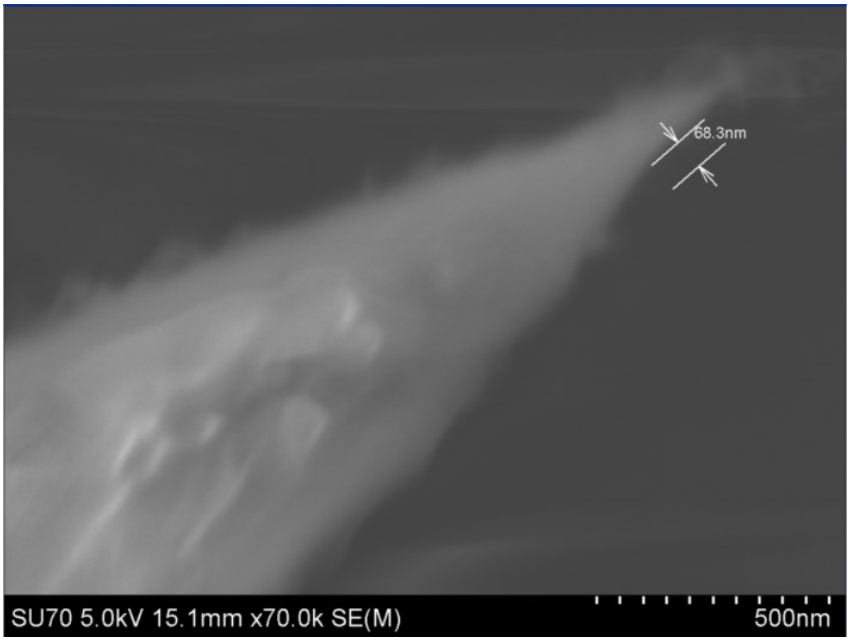

(b)

Figure 2.9 SEM image of the tapered fiber made using the static etching process. The taper length and tip diameter, were 257 μm and 68.3 nm, respectively. (a) Tapered fiber, and (b) tip of the tapered fiber.

It is clear from **Figures 2.5** and **2.9** that tapered fibers produced by both dynamic and static etching process have different characteristics. The dynamically etched fiber produced a tip with a significantly longer taper length than the statically etched taper. By using the characteristics of the tapered fibers the cone angle can be determined for both dynamically and statically etched fiber, as discussed in Section 1.2, Chapter 1. For the dynamic case, the fiber had a cladding radius of 62.5 μm, a tip radius of 42 nm, and a taper length of 2.00 mm, which produces a cone angle of 3.58°. For the static case, the fiber again had a cladding radius of 62.5 μm, but had a tip radius of 34 nm, and a taper length of 0.257 mm which produces a cone angle of 27.3°. The significance of the fiber cone angle will be discussed in Chapter 3.

2.4 Conclusions

Tapered optical fibers were produced by utilizing both the static and dynamic chemical etching processes. The fibers taper length for dynamically etched fiber was able to be calculated based on the extraction velocity from the HF, assuming the etching process was allowed to self-terminate due to the complete etching through the fiber. Statically etched tapered fiber produced a single consistent taper length and cone angle, however if the protective layer of isooctane was exchanged for some other chemical, the characteristics of the tapered fiber could be changed. The dynamically etched fibers had a significantly longer taper length, and much smaller cone angle when compared to the statically etched fibers. By changing the speed which the fiber was withdrawn from the HF for the dynamic etching process it was possible to obtain different tip characteristics.

Chapter 3

Tweezing GNRs Using the Tapered Fiber Nanoprobe

3.1 Introduction

Once the optical fiber was successfully tapered, as described in Chapter 2, it was then used in an optical tweezing experiment. Optical tweezers are traditionally built using a microscope objective which focuses a laser onto the particle of interest [54]. The purpose of optical tweezers are usually to control the movement of a nano-micron order object by keeping it trapped near the focus of the laser beam, as such optical tweezing can also be referred to as optical trapping [55]. In this research project optical tweezing was used to trap GNPs and GNRs. A metallic nanoparticle in a non-uniform electromagnetic field experiences a force due to the induced dipole moment (dipole moment per unit volume is called polarizability), which is in the direction of increased intensity, known as gradient force [56]. The nanoparticle also experiences a force due to both scattering and absorption of photons, which is very strong once the LSPR condition is satisfied as described in Chapter 1. In order to obtain optical tweezing, the gradient

force must be larger than the scattering and absorption forces exerted on the particle [56]. Highly reflective particles (such as those made of metallic material) have traditionally been difficult to trap [57]. However, it can be accomplished when the dimensions of the metallic nanoparticles are significantly less than the wavelength of light used to create the optical trap; the equations describing the maximum gradient (F_g) and scattering (F_{scatt}) forces for a small spherical metallic particle in a beam with an intensity profile described by $I(r) = I_0 \exp(-r^2/2r_0^2)$ where r_0 is the beam waist, and I_0 is the incident intensity are given below [58]

$$F_g = I_0 |\alpha| \frac{\sqrt{e}}{\varepsilon_{out} c r_0} \tag{3.1}$$

$$F_{scat} = \frac{8\pi^3 I_0 \alpha^2 \varepsilon_{out}}{3c\lambda^4} \tag{3.2}$$

Where α is the polarizability, ε_{out} is the dielectric constant of the external medium, λ is the wavelength of incident light. In this regime, the gradient force is dependent on the beam intensity and the polarizability of the particle, whereas the scattering force is dependent on the beam intensity and the square of the polarizability. The polarizability of such a particle is dependent on the particle volume, and the dielectric constants of both the particle and the medium; as the particle volume decreases the ratio between the gradient and scattering forces increases as described by the following expression [58]

$$\alpha = 3V \frac{\varepsilon_{in} - \varepsilon_{out}}{\varepsilon_{in} + 2\varepsilon_{out}} \tag{3.3}$$

where ε_{in} is the dielectric constant of the particle, and V is the volume of the particle. A more detailed description of optical tweezing can be found in reference [56]**.** It was shown by earlier research work that the evanescent waves of an optical microfiber can tweeze metallic nanoparticles [46]. In the case of research work published by Mondal et al. [46] the microfiber had a diameter of 22 μm, and the core of the multi-mode fiber was exposed to the surrounding medium which took the place of the cladding. There was sufficient evanescent wave intensity or power in the surrounding medium to facilitate optical tweezing of the metallic nanoparticles in from a colloidal solution.

3.2 Experimental Setup and Results

In order to tweeze gold nanorods (GNRs) on the surface of tapered fiber, the tapered fiber was mounted to a translation stage similar to the tapering process. A colloidal solution of metallic nanoparticles (approximately 250 μL) was then pipetted directly onto a glass slide placed beneath the tapered fiber. The metallic nanoparticles were either gold nanoparticles (GNP) (40 nm diameter, LSPR wavelength 528 nm) or Gold nanorods (GNR) (LSPR wavelength: 508 nm for transverse, and 1064 nm for longitudinal mode) in a colloidal solution. The GNP concentration provided was 0.05 mg/mL, and the GNR concentration was 0.035 mg/mL. The tapered fiber was then lowered until the tapered tip was submersed in the colloidal solution. A laser was coupled into the untapered end of the tapered fiber which was allowed to sit in the colloidal solution until the solution had completely evaporated. Three different laser wavelengths were tested in order to determine the optical tweezing properties of the chemically etched fibers. The shortest wavelength used was a 20 mW helium-neon laser at 632 nm, which

was offset from the GNP LSPR and the transverse GNR LSPR by ~ 124 nm. A 1064 nm laser diode which corresponds to the longitudinal LSPR of the GNR, but was significantly shifted from the GNP LSPR was also used at ~ 10 mW. Finally, a 1522 nm laser, which was significantly away from both of the GNR LSPR peaks, as well as the GNP LSPR peak, was used at ~ 10 mW (**Table 3.1**). Once the colloidal solution was evaporated the laser was shut off, and the tapered fiber sample was then removed and prepared for SEM characterization.

Table 3.1 Difference between laser wavelengths and GNR/GNP LSPR wavelengths used in the experiments.

Laser Wavelength	**Absolute Difference Between GNP LSPR: 528 nm**	**Absolute Difference Between GNR (Transverse) LSPR: 508 nm**	**Absolute Difference Between GNR (Longitudinal) LSPR: 1064 nm**
1522 nm	994 nm	1014 nm	458 nm
1064 nm	536 nm	556 nm	0 nm
632 nm	104 nm	124 nm	432 nm

The SEM images of the tapered fiber show several interesting characteristics. Firstly, there were little to no GNRs or GNPs present on the surface of the fiber, when dynamically or statically tapered single mode fiber (SMF 28, 8.2/125 μm) was used in the tweezing experiment. The SMF used in this experiment had an 8.2 μm core, which means the core was not exposed

until much closer to the tip of the tapered fiber compared to MMF with its 105 μm core. Additionally, the amount of power coupled into the single mode fiber was significantly less than that coupled into the multi-mode fiber. It is expected that a combination of these two factors resulted in the lack of tweezed GNPs/GNRs on the tapered SMF. A better coupling process of light into the SMF will increase the success of tweezing as shown by Mondal et al. [46].

The tweezing experiment was repeated with a dynamically etched MMF and GNPs. The GNPs were present on the surface of the fiber, and distributed randomly (**Figure 3.1, Figure 3.2, and Figure 3.3**). However, when the experiment using dynamically etched MMF was repeated for the tweezing of GNRs, there was a distinct 'grating like' distribution of alternating high and low density rings of GNRs formed on the surface of the fiber (**Figure 3.4, Figure 3.5, and Figure 3.6**). The GNR distribution was mainly found on the fiber surface between 30 μm and 7 μm fiber diameter. The MMF fiber guided many modes, but as the fiber tapers to a nano-order tip, many modes cease to propagate. Thus the field at the tip of the tapered fiber was much lower compared to that in the surrounding space. In the experiments we have seen very large concentrations of the GNRs in the diameter range of 7 μm to 30 μm, which implies that the gradient force was much lower compared to the scattering force close to the end of the tapered fiber tip. The core of the MMF was exposed to the environment, allowing the evanescent field to interact directly with the colloidal solution of GNPs or GNRs. The evanescent field produced the gradient force which optically tweezed the particles to the surface of the fiber. The interaction of the GNRs with the evanescent field also produced a scattering force, but the strength of gradient force was much larger than the scattering force, if this was not the case the GNRs would not have been drawn to the fiber surface. Preliminary theoretical investigation suggests that the evanescent waves of the fundamental and higher order modes interfere, and

produce an interference pattern along the length of the tapered fiber [59]. Because the GNRs are anisotropic and had two LSPR frequencies, the interaction of the electric field would be polarization dependant, as opposed to the GNPs which were isotropic; which lead to the different deposition patterns between the two particles. The location of a high intensity zone created a larger gradient force compared to the sections with a low intensity zone. The experiment was repeated with no laser light, and in each case there were no GNRs present on the surface of the tapered fiber, except for a few cases where a small cluster of nanorods was found in a single spot with no apparent distribution pattern, which could be due to an electrostatic force between GNR and silica.

Finally, when the experiment was repeated with statically etched MMF there were no observable GNRs or GNPs on the surface of the fiber. This was due to the difference in cone angles of the dynamically and statically etched fibers, as the intensity of the evanescent wave is dependent on the cone angle. In dynamically etched fibers the cone angle was extremely shallow, 3.58° as described in Chapter 2, whereas the statically etched fiber had a considerably larger cone angle of 27.3°. Vobornik et al [60] described how tapered fiber will guide more modes closer to the tip if the cone angle of the tapered fiber is larger. For a small cone angle fiber fewer modes are successfully guided to the tip of the fiber, which means they are lost to the environment.

Since the cladding of the fiber was etched away the core is exposed to the environment. The core itself is also tapered down to a nanometer order tip diameter. The confinement of the mode field distribution is proportional to the V parameter of the fiber, which is directly proportional to the core radius. So as the core diameter decreases, the number of modes which can be confined within the fiber also decreases. Further, a smaller V number means a loosely

confined electric filed and larger evanescent field. These evanescent waves in the tapered region induce a gradient force and thus tweeze the nanoparticles on the surface of the tapered fiber. In tapered fiber once the cladding is etched away, the refractive index can be replaced by the index of the surrounding medium.

GNPs were successfully tweezed at three laser wavelengths, 1522 nm (**Figure 3.1)**, 1064 nm (**Figure 3.2**), and 632 nm (**Figure 3.3**)**.** There was no notable change in their distribution pattern between wavelengths. For GNRs however there was a notable difference in the appearance of the GNR distribution pattern when the off resonance 1522 nm laser was used for optical tweezing (**Figure 3.4**), compared to 1064 nm (**Figure 3.5**) and 632 nm (**Figure 3.6**)**.** In the case of tweezing with the 1522 nm laser, the rings appear much more distinct. Optical tweezing requires the gradient force to be greater than the scattering and absorption force, so tweezing using a laser that is off resonance will give better results. The scattering and absorption is maximum at the LSPR wavelength as described in Chapter 1.

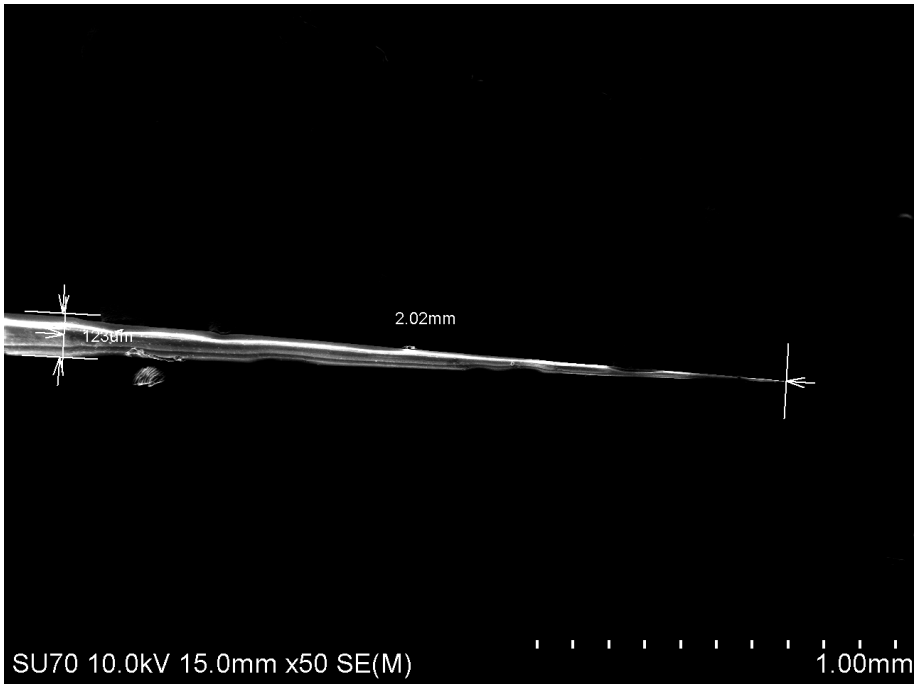

(a)

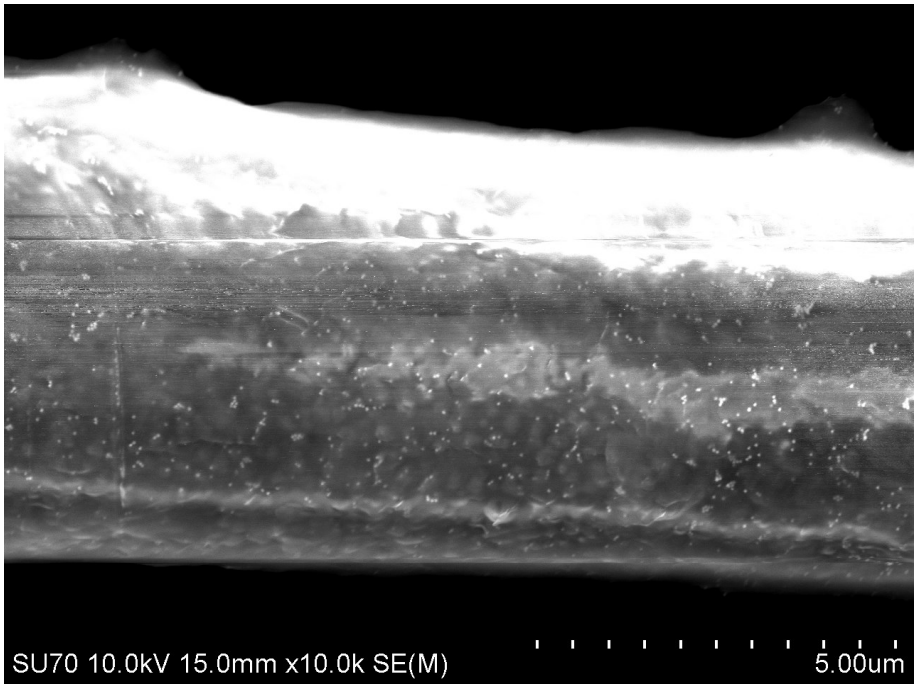

(b)

Figure 3.1 Dynamically etched MMF with a taper length of 2.02 mm tweezed with GNP at a laser wavelength of 1522 nm. (a) GNP covered tapered fiber, and (b) is a magnified portion of the tapered fiber to show GNP distribution.

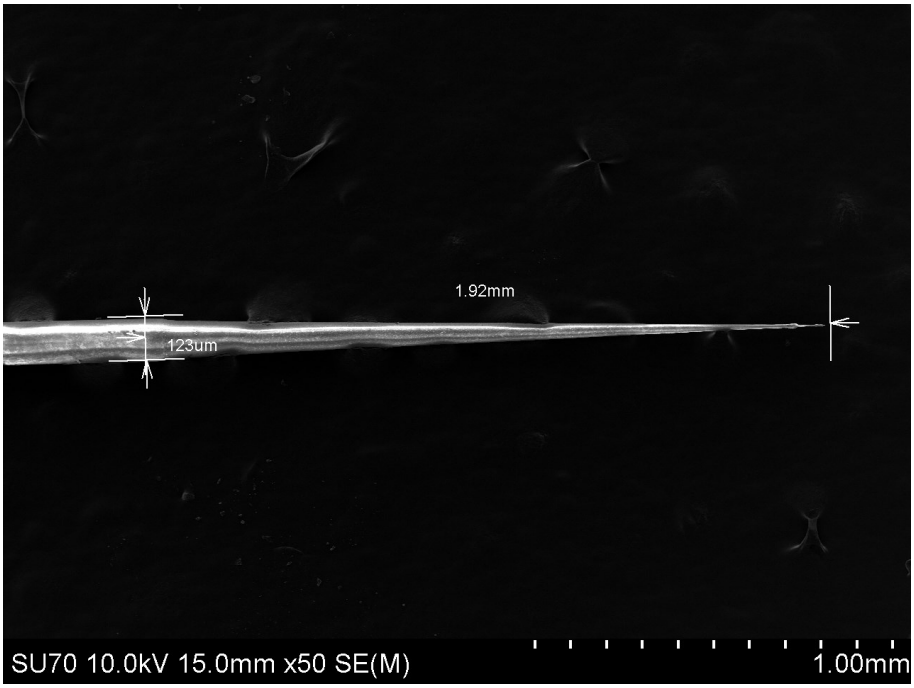

(a)

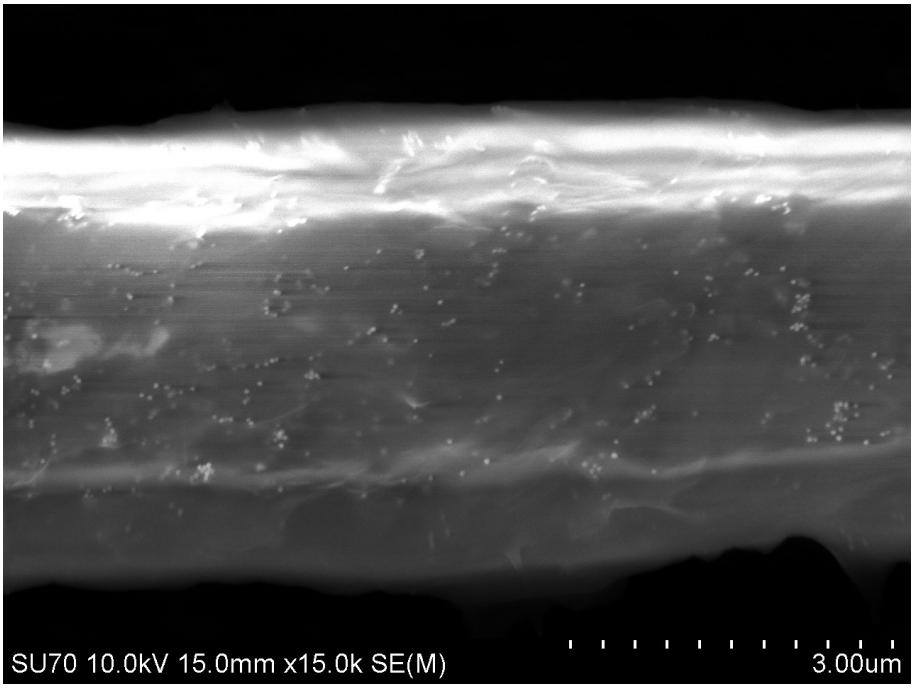

(b)

Figure 3.2 Dynamically etched MMF with a taper length of 1.92 mm tweezed with GNP at a laser wavelength of 1064 nm. (a) Tapered fiber covered with GNP, and (b) is a magnified portion of the tapered fiber covered with GNP distribution.

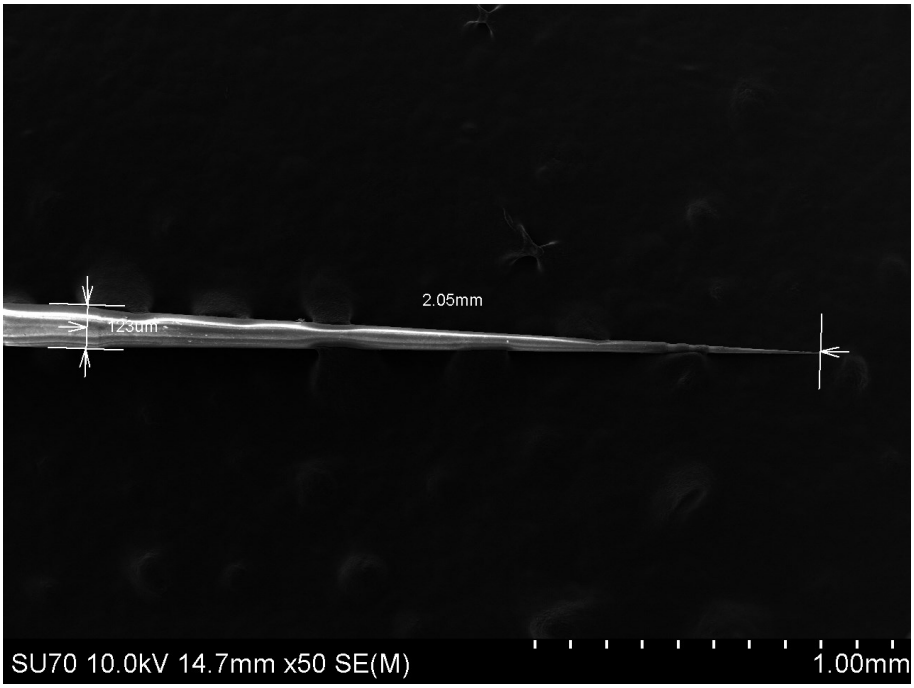

(a)

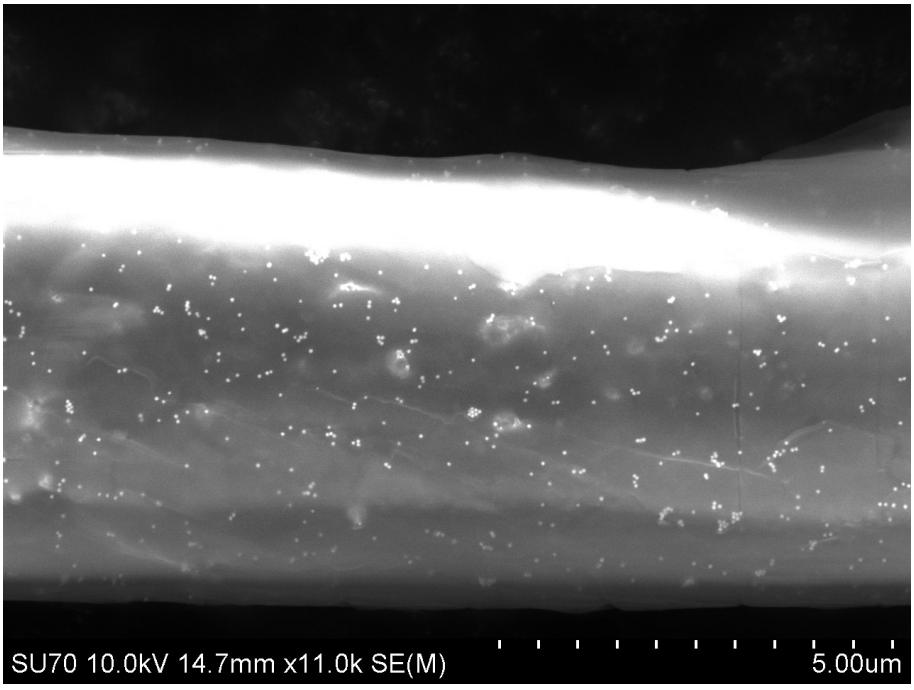

(b)

Figure 3.3 Dynamically etched MMF with a taper length of 2.05 mm tweezed with GNP at a laser wavelength of 632 nm. (a) Tapered fiber covered with GNP, and (b) is a magnified portion of the tapered fiber covered with GNP distribution.

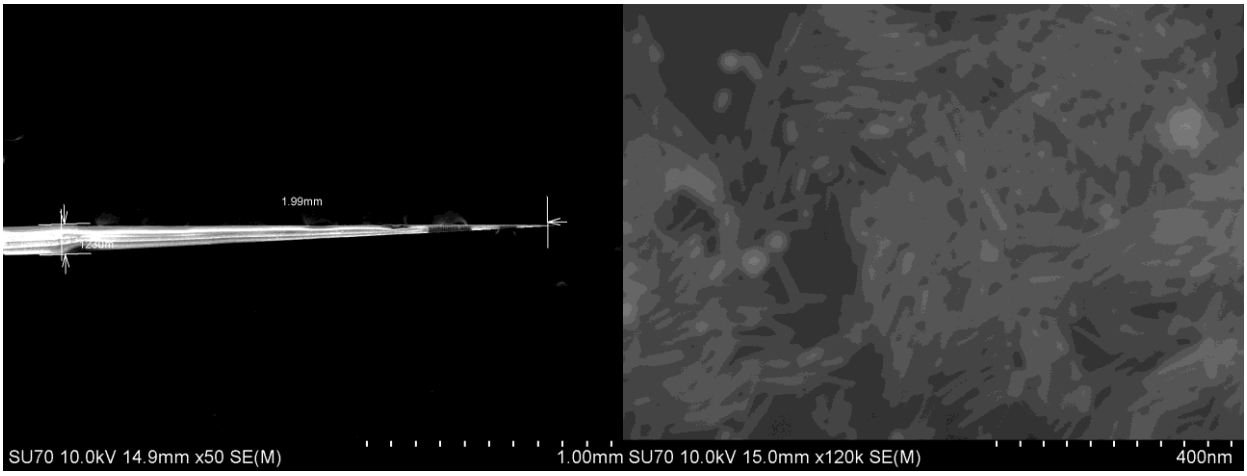

(a) (b)

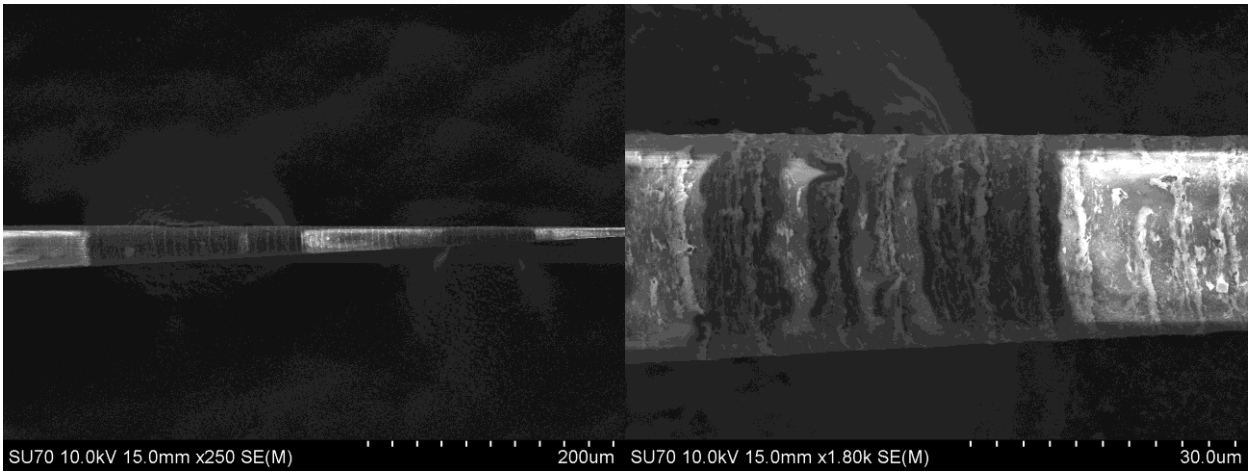

(c) (d)

Figure 3.4 Dynamically etched MMF with a taper length of 1.99 mm tweezed with GNR using a 1522 nm laser. (a) Tapered fiber; (b) GNRs distribution on the magnified section of the tapered fiber; (c) Grating pattern on the tapered fiber due to GNRs; and (d) is a magnified section of the grating like distribution.

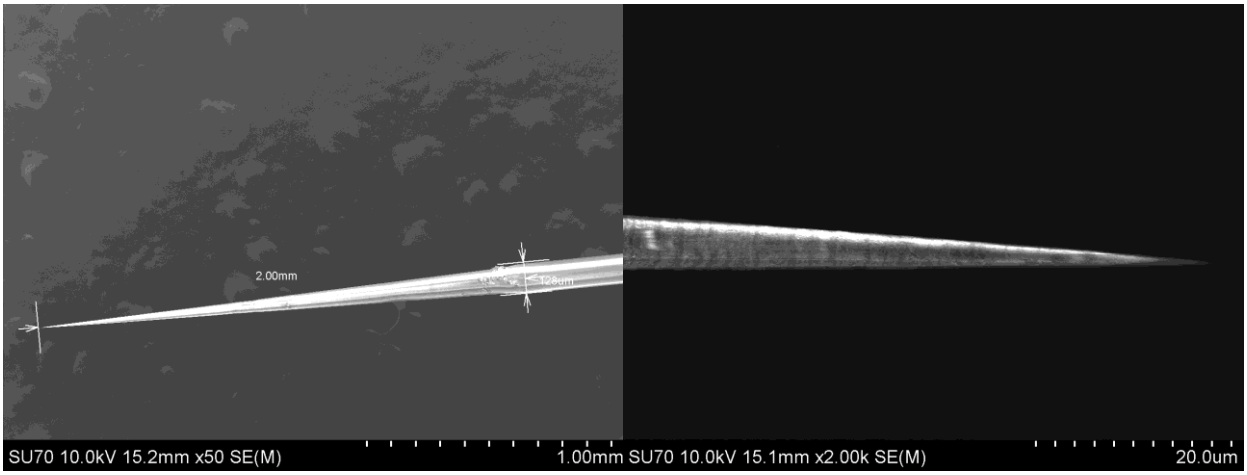

(a) (b)

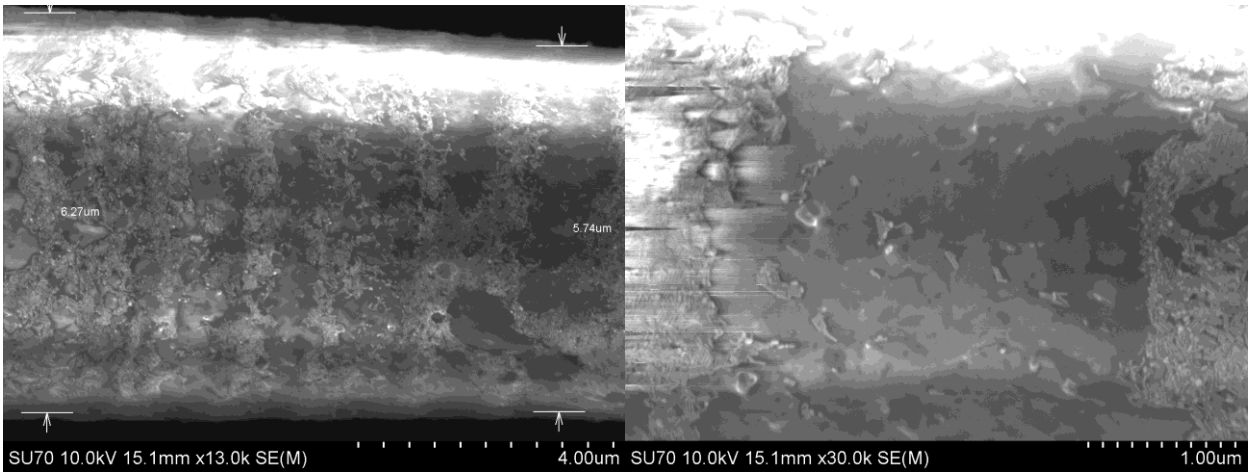

(c) (d)

Figure 3.5 Dynamically etched MMF with a taper length of 2.00 mm tweezed with GNR using a 1064 nm laser. (a) Tapered fiber; (b) GNRs distribution on the magnified section of the tapered fiber; (c) Grating pattern on the tapered fiber due to GNRs; and (d) is a magnified section of the grating likes distribution.

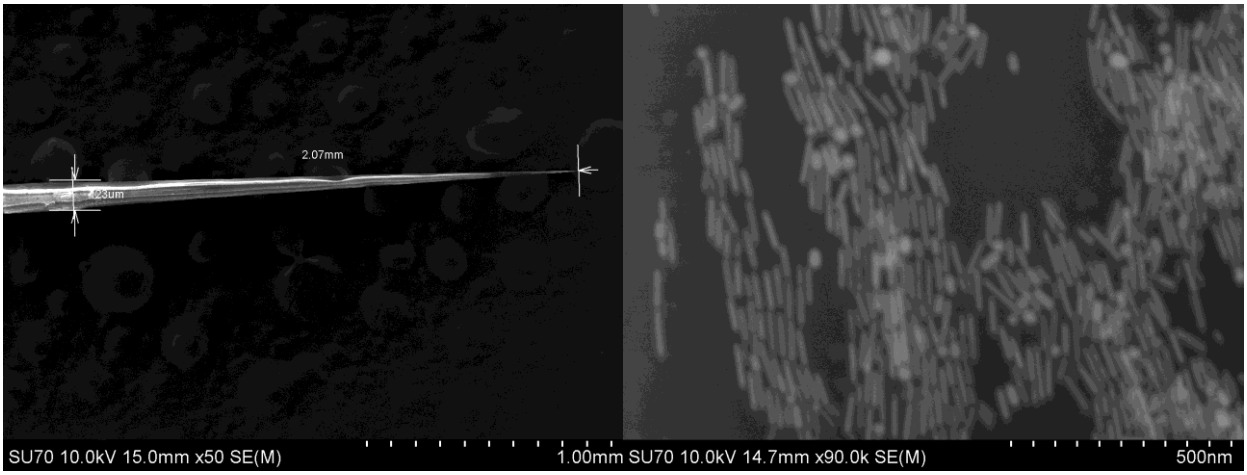

(a) (b)

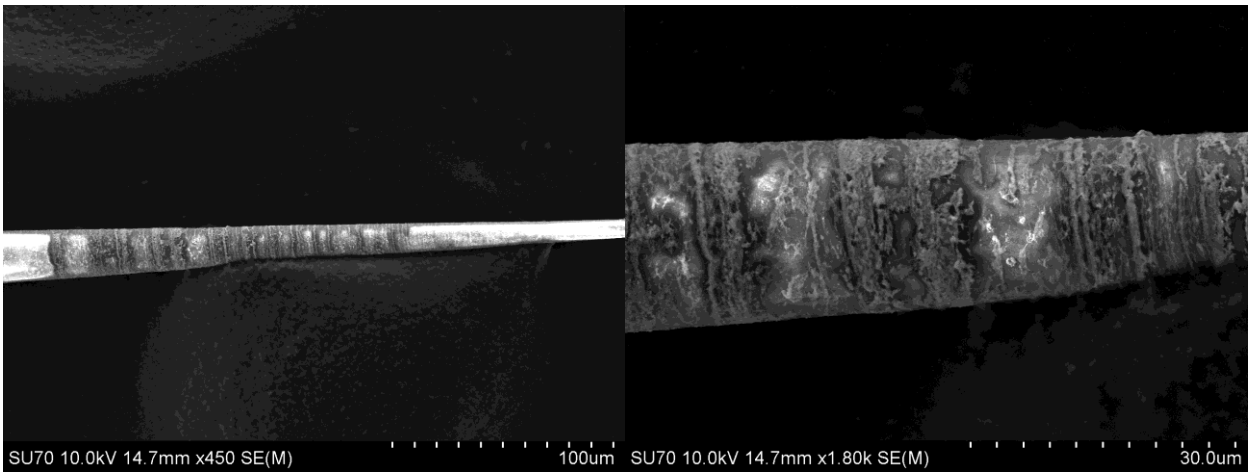

(a) (b)

Figure 3.6 Dynamically etched MMF with a taper length of 2.07 mm tweezed with GNR using a 632 nm laser. (a) Tapered fiber; (b) GNRs distribution on the magnified section of the tapered fiber; (c) Grating pattern on the tapered fiber due to GNRs; and (d) is a magnified section of the grating likes distribution.

It was observed that in a special case of statically etched MMF, GNRs could be tweezed onto the tapered tip when the etching process was terminated prematurely. In this case (**Figure 3.7**) the statically etched fiber was withdrawn from the HF before it had been completely etched through by the HF acid. This resulted in an elongated, syringe like, tip. See **Figure 2.6** from Chapter 2 to compare a normal statically etched MMF to the prematurely terminated tip (**Figure 3.7**). The GNRs observed on the fiber were only observed on this elongated tip, not on the main tapered structure.

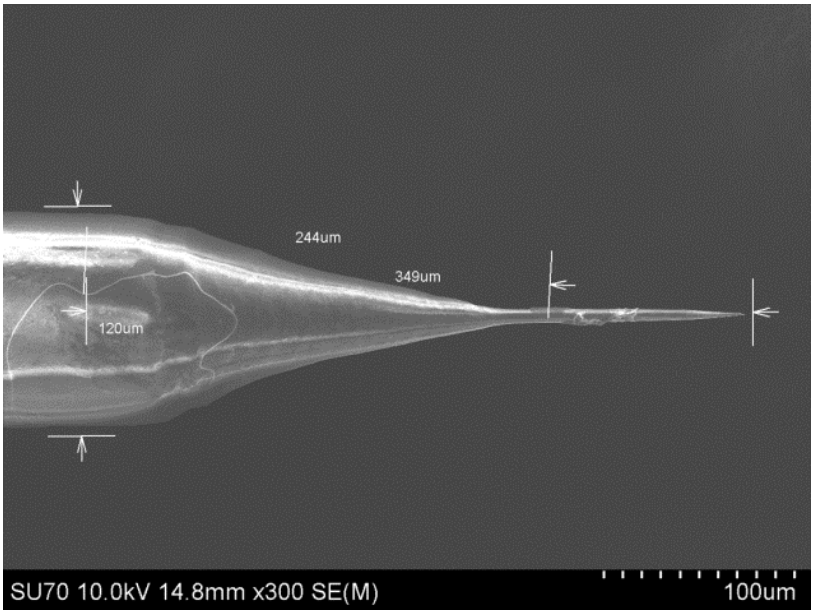

(a)

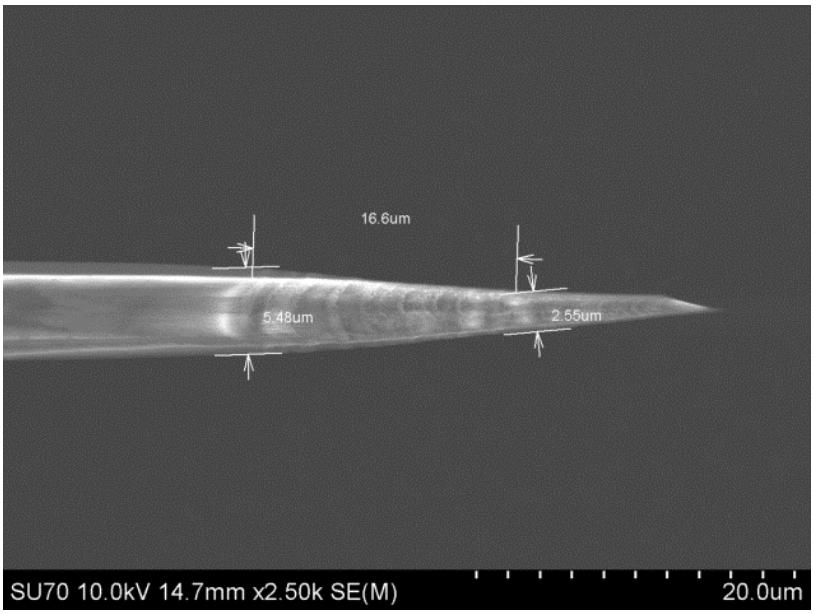

(b)

Figure 3.7 Prematurely terminated statically etched MMF tweezed with GNR using a 1064 nm laser with an extended taper length of 0. 346 mm. (a) The tapered fiber, and (b) distribution of GNR rings near tip.

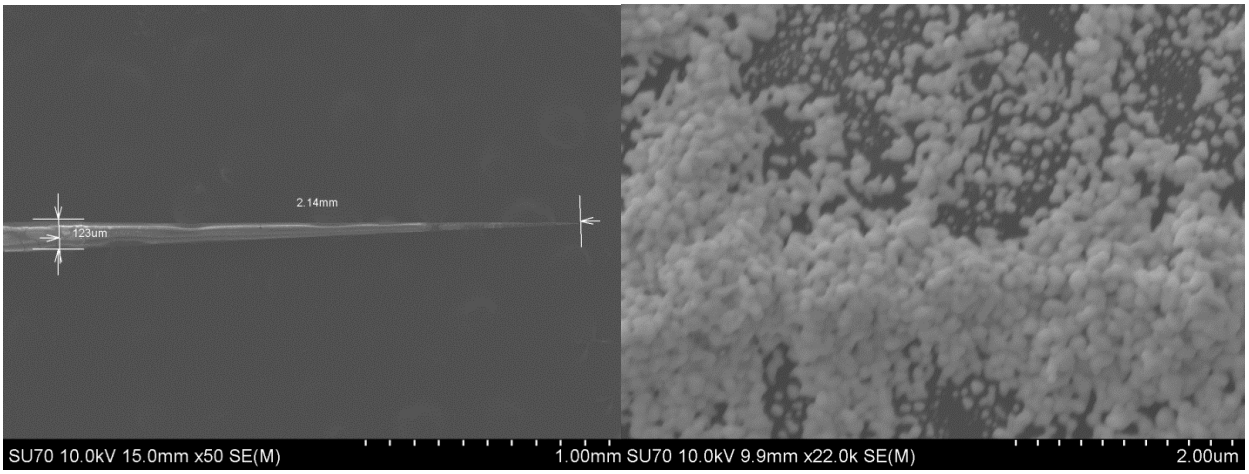

(a) (b)

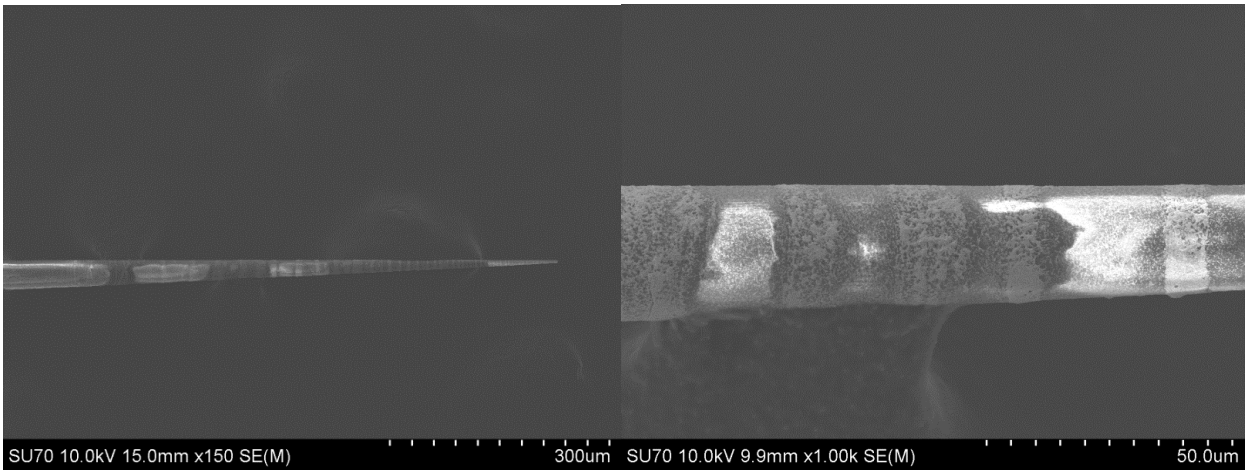

(c) (d)

Figure 3.8 Dynamically etched MMF with a taper length 2.14 mm, used to tweeze GNRs at 1522 nm, 100 mW power. (a) Tapered fiber; (b) didtribution of GNRs (destroyed); (c) grating like distribution of GNRs at the tapered end; and (d) grating pattern.

Figure 3.8 shows a fiber which was used for optically tweezing GNRs, again at 1522 nm, but this time at ~100 mW power. The result was again consistent with what we had seen previously, a ring distribution of alternating high and low densities, but in this case the GNRs had been completely destroyed. The destruction of GNRs at high laser power has been previously reported [61].

3.3 Conclusions

When optical tweezing was performed using dynamically etched MMF both GNRs and GNPs were consistently found on the fiber surface. Three different laser wavelengths were used to perform optical tweezing, which were both near and far from the LSPR wavelength condition of the GNRs and GNPs; tweezing was successful with all three. No noticeable change was observed in the random distribution of GNPs between laser wavelengths. When GNRs were tweezed they formed a grating like pattern on the surface of the tapered fiber. The rings which formed on the fiber were much more distinct when 1522 nm was used to tweeze when compared to the other two laser wavelengths used. The ring spacing was non-uniform along the length of the fiber. Statically etched MMF did not successfully tweeze either GNPs or GNRs. There was a condition where statically etched fiber did successfully tweeze GNRs, but it required that the etching process was terminated early which resulted in an elongated needle like tip at the end of the tapered fiber; GNR rings were found on this elongated tip. Neither dynamically or statically etched SMF successfully tweezed GNPs or GNRs. If tweezing was attempted at high power the GNRs or GNPs would be destroyed; however for GNRs the distinct grating like pattern was still observed on the surface of the fiber.

Chapter 4

Application of the Tapered Fiber as a Sensor

4.1 Introduction

The potential uses of tapered optical fiber with a metallic nanostructure are quite promising. It is anticipated that the probe will be able to function as a Surface Enhanced Raman Spectroscopy (SERS) substrate. SERS enhancement, as described in Chapter 1, requires a roughened metallic substrate in order to enhance the detected Raman signal [62]. As seen in Chapter 3, the GNRs tweezed onto the surface of the fiber form distinct rings, where the rings are formed by a layer of GNRs.

It has been demonstrated that nanoparticles of various sizes and shapes can act as a SERS substrate such as: 15 nm and 35 nm diameter [63] as well as 32 and 73 nm diameter [64] gold nanoparticles deposited on a glass slide, gold nanoparticles (150 nm diameter), gold nanotriangles (120 nm long), and gold nanostars (150 nm long) deposited on a calcium fluoride substrate [13], silver nanoparticles with diameters ranging from 10 to 50 nm deposited on a

silicon wafer [65], gold nanorods (45 nm long 11 nm wide) deposited on silicon wafers [66], additionally, silver nanoparticles (50 nm diameter) deposited on the face of an optical fiber tip via chemical deposition methods [67].

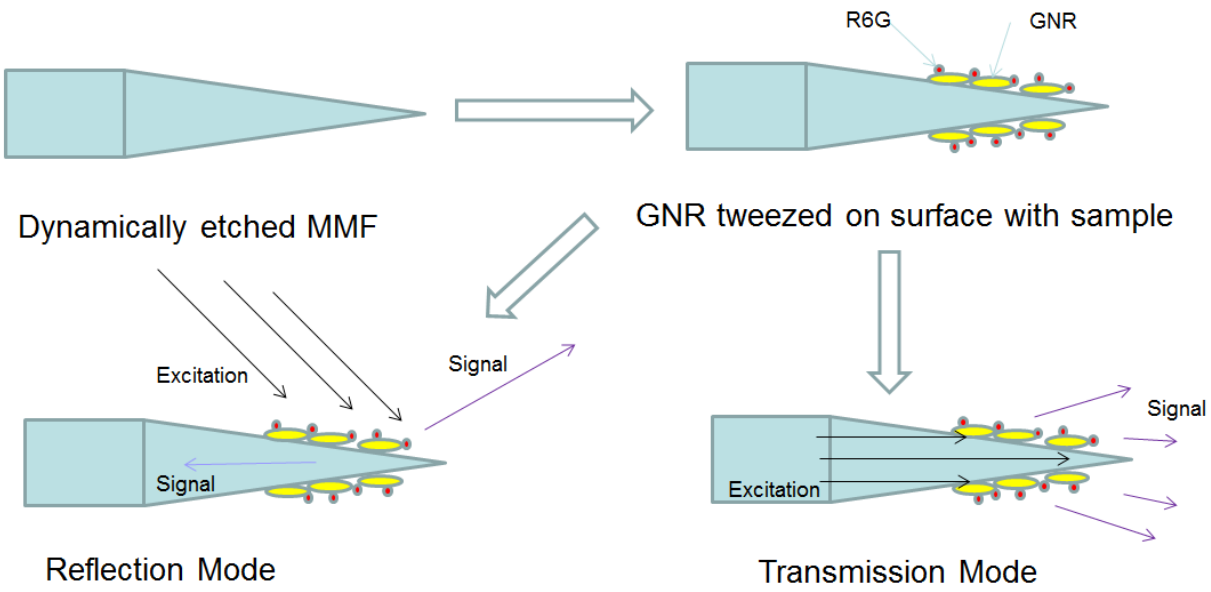

Figure 4.1 Nano-probe used as a Raman probe. Rhodamine 6G (R6G, 99% pure Sigma Aldrich), GNR of aspect ratio ~6.7. A dynamically etched fiber is tweezed with GNRs and has a sample (R6G) applied to it, it is then excited by either an external laser, or by a laser coupled to the untapered end of the fiber. The resultant signal is then collected.

Figure 4.1 depicts the use of the nano-probe for Raman signal detection. Starting with the top left fiber, an untweezed tapered MMF is shown. This tapered fiber is then tweezed with GNRs and a R6G sample is applied to the fiber. The Raman signal can be stimulated in two different ways. The first, as seen in the bottom left, is by reflection mode. In reflection mode an

external laser is used for excitation of the Raman signal, the resultant signal can either be collected as it scatters away from the fiber. The second method to stimulate the Raman signal is transmission mode. For transmission mode, the laser used to excite the signal is coupled into the untapered end of the fiber, and the resulting scattered light is collected from the tapered end of the fiber.

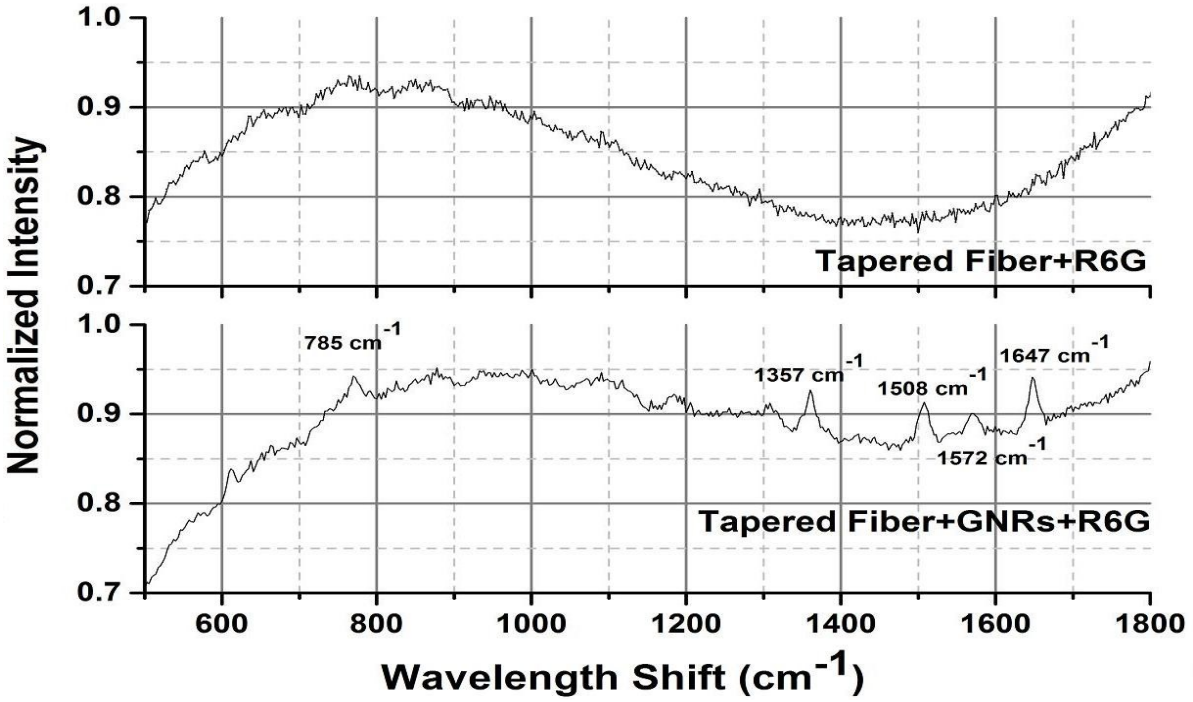

Figure 4.2 Reflection mode: laser at 532 nm, scattered light was collected using a Raman spectrometer (Renishaw). Comparing the spectrum obtained using reflection mode from a Tapered fiber with and without a GNR structure.

In order to incorporate R6G (99%, Sigma Aldrich) on the tapered fiber, the colloidal GNR solution was saturated with R6G before optical tweezing. Once tweezing was completed

the tapered fiber was covered with both GNRs and R6G. **Figure 4.2** shows the spectra obtained using reflection mode for a R6G covered tapered fiber with and without GNRs. For the reflection mode, a laser at 532 nm was used for excitation. The laser beam was incident on the tapered section of the fiber covered with R6G and the scattered light was collected. Both stimulation and collection were achieved using a Raman spectrometer (inVia Raman microscope). The reflection mode spectrum has multiple identifiable peaks, which are consistent with the expected peak locations for R6G. After the metallic nanostructure was developed using the method described in chapter 2, R6G powder was sprinkled on the tapered fiber. The fiber without GNRs was covered with R6G using the same procedure. In both cases a 532 nm laser was used, which corresponds to the transverse plasmon resonance wavelength of the GNR. It is clear from **Figure 4.2** that the fiber with plasmonic structure produced the characteristic spectrum for R6G. The peaks labelled on the reflection spectrum correspond very well with previously reported SERS spectra for Rhodamine 6G [68]. The peak at 1647 cm^{-1} corresponds to an in plane C-H bend and a xanthene ring stretch, 1572 cm^{-1} corresponds to an in plane N-H bend and a xanthene ring stretch, the peak at 1508 cm^{-1} corresponds to a C-N stretch, a C-H bend, and a xanthene ring stretch, 1357 cm^{-1} corresponds to an in plane C-H bend, an a xanthene ring stretch, and 785 cm^{-1} corresponds to an out of plane C-H bend [69].

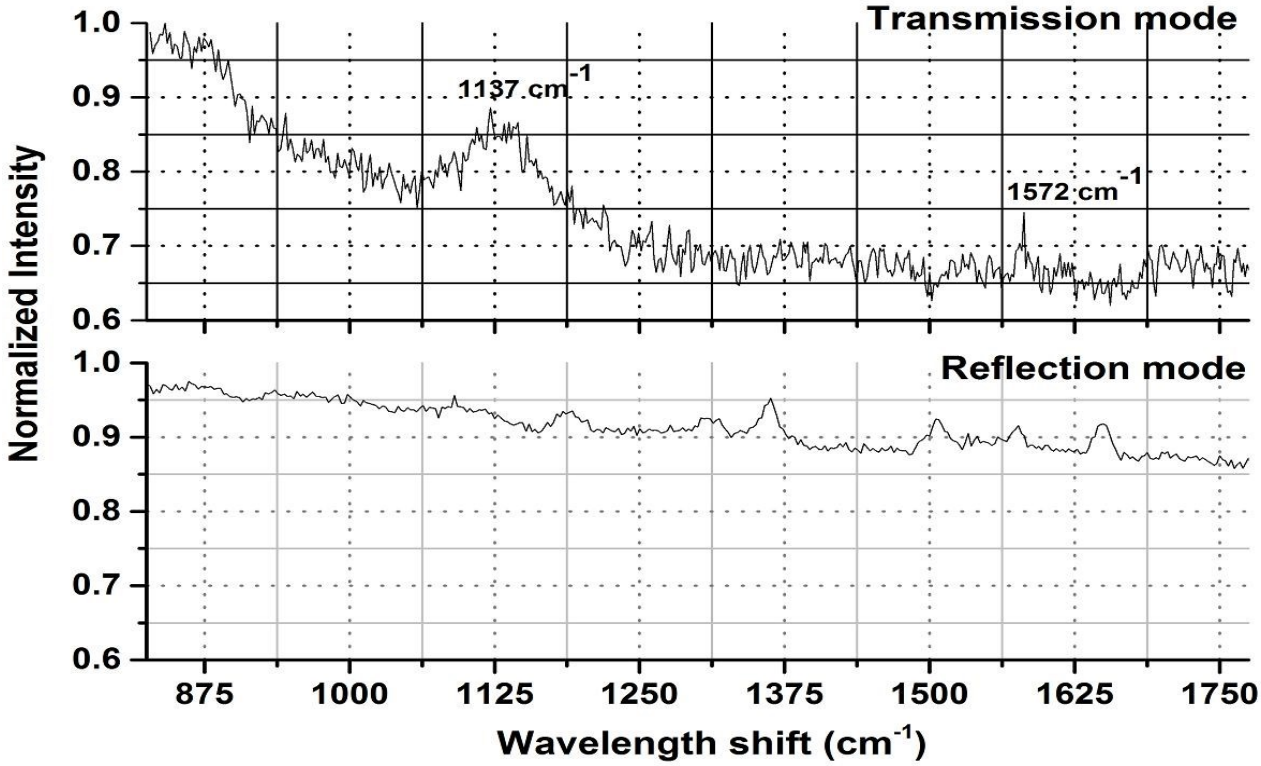

Figure 4.3 Top: A 1064 nm diode laser (200 mW) was coupled to the un-tapered end of the tapered MMF. The light from the tapered end of the fiber was analysed by an iHR 550 spectrometer, with a CCD camera attached. Bottom: Results using the Reflection mode.

Figure 4.3 is the spectrum obtained for R6G via two different methods. For transmission mode a 1064 nm diode laser with 200 mW was coupled to the un-tapered end of the tapered MMF. The light from the tapered end of the fiber was analysed by an iHR 550 spectrometer, with a Synapse CCD camera attached. In order to collect the light the tapered end of the fiber was aligned with the entrance slit of the spectrometer. A notch filter (1064 nm) was placed between the tapered fiber and the entrance slit as shown in **Figure 4.4.** Reflection mode was also used with the same spectrometer setup. It is clear from the spectra that the number of peaks

obtained may differ depending on both the method of collection and the excitation wavelength used. The transmission mode spectrum was obtained using a 1064 nm laser, which is the longitudinal plasmon resonance wavelength of the GNRs. We were able to obtain a large peak at 1137 cm^{-1}, which was absent in the reflection mode spectrum. The peak at 1572 cm^{-1} was present in both reflection and transmission mode spectra. both peaks correspond with previously reported SERS spectra for Rhodamine 6G [68]. The peak at 1137 cm^{-1} corresponds to the motion of the xanthene ring as well as the NHC_2H_5 group [70].

Future work with this nanoprobe will be done in coordination with Dr. Linhananta, who is an expert in biological physics specialising in proteins. The potential of using this probe for protein detection, particularly proteins which are associated with cancer or other diseases, utilizing SERS will be investigated. Proteins have been detected using nanoparticles as a SERS substrate before [71;72], however achieving this with our substrate and probe design would be a testament to its effectiveness.

(a)

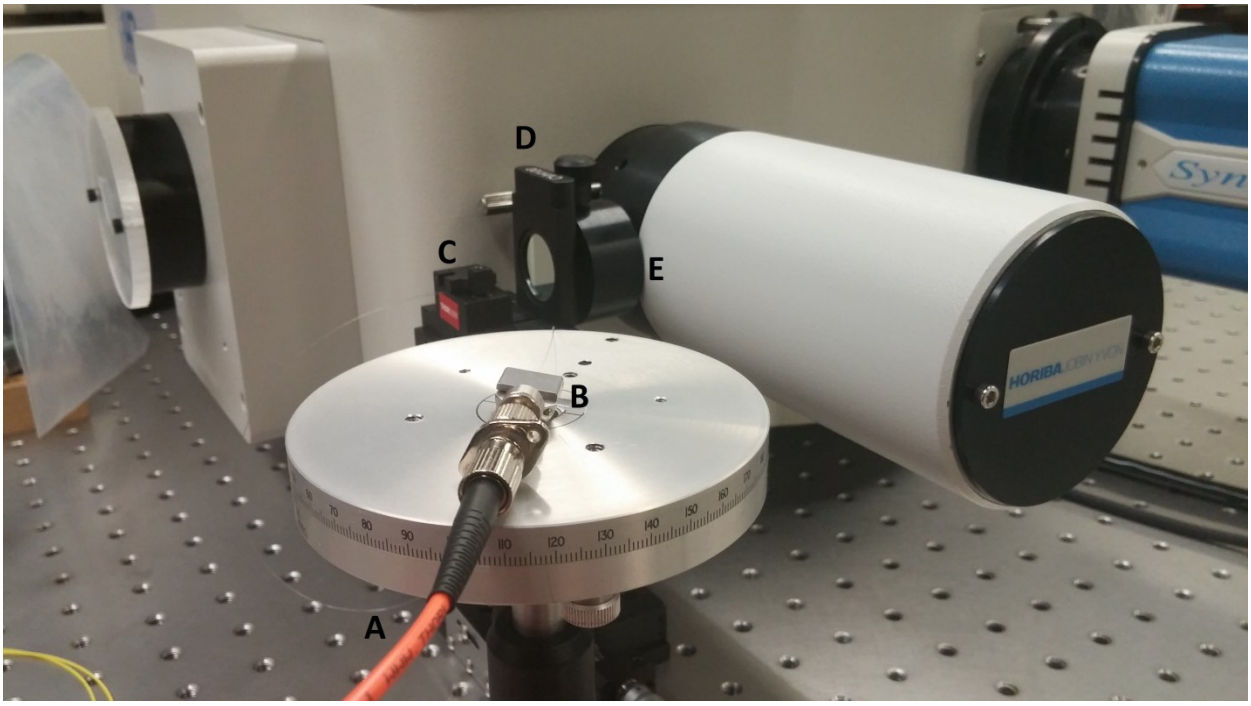

(b)

Figure 4.4 (a): full profile view of the iHR 550 spectrometer used for the detection of the transmission mode signal. (b): Close up of the entrance of the IHR 550 spectrometer, where "A" is the MMF coupled on one end to a 1064 nm laser, and coupled in the image to the untapered end of the tapered optical fiber, "B". "C" is the tapered end of the optical fiber aligned with the entrance slit "E" with a 1064 nm notch filter "D" in between.

4.2 Conclusion

In conclusion, we have shown that the tapered MMF coated with periodic distribution of GNRs can be used as a SERS substrate either in the reflection or transmission modes. Because of the periodic GNR distribution, the scattered light can be coupled very easily; in fact, the same fiber can be used for both transmitting laser light to excite the chemical adsorbed on the GNRs and for collecting the scattered light. The mechanism behind the separation between two circular rings of GNRs will be investigated in more detail in the future, along with its potential impact on the optical properties of the tapered fiber probe. The GNPs had a concentration of 0.05 mg/mL whereas the GNRs had a concentration of 0.035 mg/mL when in the colloidal solution before tweezing, however the amount deposited on the fibers surface after tweezing was significantly less, and the distribution had no observable pattern. The reason for this will be investigated in the future; however the theory behind optical tweezing suggests that the gradient force must be larger than the scattering force. As discussed in Chapter 1, GNPs and GNRs have different optical properties, especially when considering their LSPR wavelength; GNRs have two resonance wavelengths whereas GNPs only have one. Furthermore, the proximity of the excitation laser wavelength to the LSPR wavelength will affect the scattering and absorption forces on the particle; thus the evanescent field has a different interaction with the GNPs compared to the GNRs.

The benefit of using this probe design comes down to two things; cost of production, and potential ease of use. In terms of production cost of the raw materials and their assembly, the probe simply consists of a MMF, and a small volume of colloidal GNR solution is required for optical tweezing onto the surface of the fiber, along with the HF and organic solvent required to make the tapered fiber itself. We have demonstrated that a laser within a large range of

operating wavelengths (632 nm to 1522 nm tested) can be used to produce the distinct ring like pattern, so any general laser should be sufficient. This means that the cost of manufacturing the SERS substrate from setup to probe material is very minimal.

References

[1] G. Keiser, *Optical Fiber Communications*, 3 ed. Boston, MA: McGraw Hill, 2000.

[2] A. W. Snyder and J. D. Love, *Optical Waveguide Theory* Chapman and Hall Ltd, 1983.

[3] D. Gloge, "Weakly guiding fibers," *Appl. Opt.*, vol. 10, no. 10, pp. 2252-2258, Oct.1971.

[4] O. Strobel, *Optical and Microwave Technologies for Telecommunication Networks* John Wiley & Sons, 2016.

[5] J. Noda, K. Okamoto, and Y. Sasaki, "Polarization-Maintaining Fibers and Their Applications," *Journal of Lightwave Technology*, vol. 4, no. 8, pp. 1071-1089, Aug.1986.

[6] G. A. Valaskovic, M. Holton, and G. H. Morrison, "Parameter control, characterization, and optimization in the fabrication of optical fiber near-field probes," *Applied Optics*, vol. 34, no. 7, pp. 1215-1228, 1995.

[7] Y. K. Cheong, K. S. Lim, W. H. Lim, W. Y. Chong, and R. Zakaria, "Fabrication of tapered fibre tip using mechanical polishing method," *Review of Scientific Instruments*, vol. 82, pp. 086115-1-086115-3, 2011.

[8] H. Nikbakht, H. Latifi, M. Oraie, and T. Amini, "Fabrication of tapered tip fibers with a controllable cone angle using dynamical etching," *Journal of Lightwave Technology*, vol. 33, no. 23, pp. 4707-4711, 2015.

[9] R. Muller and C. Lienau, "Three-dimensional analysis of light propagation through uncoated near-field fibre probes," *Journal of Microscopy*, vol. 202, no. 2, pp. 339-346, 2001.

[10] U. Kreibig and C. V. Fragstein, "The Limitation of Electron Mean Free Path in small silver particles," *Zeitschrift Fur Physik*, vol. 224, pp. 307-323, 1969.

[11] R. Narayanan and M. A. El-Sayed, "Catalysis with transition metal nanoparticles in colloidal solution: nanoparticle shape dependence and stability," *Journal of Physical Chemistry B*, vol. 109, no. 26, pp. 12663-12676, 2005.

[12] C. L. Haynes, A. J. Haes, A. D. McFarland, and R. P. Van Duyne, "Nanoparticles with tunable localized surface plasmon resonances," *Topics in Fluorescence Spectroscopy*, vol. 8, pp. 47-99, 2005.

[13] F. Tian, F. Bonnier, A. Casey, A. E. Shanahan, and H. J. Byrne, "Surface enhanced Raman scattering with gold nanoparticles: effect of particle shape," *Analytical Methods*, vol. 6, pp. 9116-9123, 2014.

[14] G. Doria, J. Conde, B. Veigas, L. Giestas, C. Almeida, M. Assuncao, J. Rosa, and P. V. Baptista, "Noble metal nanoparticles for biosensing applications," *Sensors*, vol. 12, pp. 1657-1687, 2012.

[15] D. K. Chatterjee, P. Diagaradjane, and S. Krishnan, "Nanoparticle-mediated hyperthermia in cancer therapy," *Theraputic Delivery*, vol. 2, no. 8, pp. 1001-1014, 2011.

[16] X. Lu, M. Rycenga, S. Skrabalak, B. Wiley, and Y. Xia, "Chemical synthesis of novel plasmonic nanoparticles," *Annual Review of Physical Chemistry*, vol. 60, pp. 167-192, 2009.

[17] J. N. Anker, W. P. Hall, O. Lyandres, N. C. Shah, J. Zhao, and R. P. Van Duyne, "Biosensing with plasmonic nanosensors," *Nature Materials*, vol. 7, no. 6, pp. 442-453, June2008.

[18] S. Link and M. A. El-Sayed, "Shape and size dependence of radiative, non-radiative and photothermal properties of gold nanocrystals," *International Reviews in Physical Chemistry*, vol. 19, no. 3, pp. 409-453, 2000.

[19] L. M. Liz-Marzan, "Tailoring surface plasmons through the morphology and assembly of metal nanoparticles," *Langmuir*, vol. 22, no. 1, pp. 32-41, 2006.

[20] E. Petryayeva and U. J. Krull, "Localized surface plasmon resonance: nanostructures, bioassays and biosensing-a review," *Analytica Chimica Acta*, vol. 706, pp. 8-24, 2011.

[21] M. Hu, J. Chen, Z. Li, L. Au, G. Hartland, X. Li, M. Marquez, and Y. Xia, "Gold nanostructures: engineering their plasmonic properties for biomedical applications," *Chemical Society Reviews*, vol. 35, pp. 1084-1094, 2006.

[22] T. R. Jensen, M. D. Malinsky, C. L. Haynes, and R. P. Van Duyne, "Nanosphere lithography: tunable localized surface plasmon resonance spectra of silver nanoparticles," *Journal of Physical Chemistry B*, vol. 104, no. 45, pp. 10549-10556, 2000.

[23] S. A. Maier and H. A. Atwater, "Plasmonics: localization and guiding of electromagnetic energy in metal/dielectric structures," *Journal of Applied Physics*, vol. 98, pp. 011101-1-011101-10, 2005.

[24] K. A. Willets and R. P. Van Duyne, "Localized surface plasmon resonance spectroscopy and sensing," *Annual Review of Physical Chemistry*, vol. 58, pp. 267-297, 2007.

[25] C. L. Haynes and R. P. Van Duyne, "Plasmon scanned surface-enhanced Raman scattering excitation profiles,", 728 ed 2002, p. S10.7.1-S10.7.6.

[26] P. Stoller, V. Jacobsen, and V. Sandoghdar, "Measurment of the complex dielectric constant of a single gold nanoparticle," *Optics Letters*, vol. 31, no. 16, pp. 2474-2476, 2006.

[27] P. Rostron, S. Gaber, and D. Gaber, "Raman spectroscopy, a review," *International Journal of Engineering and Technical Research*, vol. 6, no. 1, pp. 50-64, 2016.

[28] A. Kudelski, "Analytical applications of Raman spectroscopy," *Talanta*, vol. 76, pp. 1-8, 2008.

[29] E. C. Le Ru, E. Blackie, M. Meyer, and P. G. Etchegoin, "Surface enhanced Raman scattering enhancement factors: a comprehensive study," *Journal of Physical Chemistry C*, vol. 111, no. 37, pp. 13794-13803, Sept.2007.

[30] M. Moskovits, "Surface-enhanced Raman spectroscopy:a brief retrospective," *Journal of Raman Spectroscopy*, vol. 36, pp. 485-496, 2005.

[31] P. L. Stiles, J. A. Dieringer, N. C. Shah, and R. P. Van Duyne, "Surface-enhanced Raman spectroscopy," *Annual Review of Analytical Chemistry*, vol. 1, pp. 601-626, 2008.

[32] G. C. Schatz and R. P. Van Duyne, "Electromagnetic mechanism of surface-enhanced spectroscopy," in *Handbook of Vibrational Spectroscopy* 2002.

[33] M. K. Hossain, Y. Kitahama, G. G. Huang, X. Han, and Y. Ozaki, "Surface-enhanced Raman scattering: realization of localized surface plasmon resonance using unique substrates and methods," *Analytical and Bioanalytical Chemistry*, vol. 394, pp. 1747-1760, 2009.

[34] T. A. El-Brolossy, T. Abdallah, M. B. Mohamed, S. Abdallah, K. Easawi, S. Negm, and H. Talaat, "Shape and size dependence of the surface plasmon resonance of gold nanoparticles studied by photoacoustic technique," *European Physical Journal Special Topics*, vol. 153, pp. 361-364, 2008.

[35] P. Geshev, S. Klein, and M. Hietschold, "Calculation of the electric-field enhancement at nanoparticles of arbitrary shape in close proximity to a metallic surface," *Physical Review B*, vol. 70, pp. 075402-1-075402-16, 2004.

[36] X. H. Huang, S. Neretina, and M. A. El-Sayed, "Gold Nanorods: From Synthesis and Properties to Biological and Biomedical Applications," *Advanced Materials*, vol. 21, no. 48, pp. 4880-4910, Dec.2009.

[37] I. Ros, T. Placido, V. Amendola, C. Marinzi, N. Manfredi, R. Comparelli, M. Striccoli, A. Agostiano, A. Abbotto, D. Pedron, R. Pilot, and R. Bozio, "SERS properties of gold nanorods at resonance with molecular, transverse, and logitudinal plasmon excitations," *Plasmonics*, vol. 9, pp. 581-593, 2014.

[38] J. Tao, Y.-H. Lu, R.-S. Zheng, K.-Q. Lin, Z.-G. Xie, Z.-F. Luo, S.-L. Li, P. Wang, and H. Ming, "Effect of aspect ratio distribution on localized surface plasmon resonance extinction spectrum of gold nanorods," *Chinese Physics Letters*, vol. 25, no. 12, pp. 4459-4462, 2008.

[39] C. J. Murphy and C. J. Orendorff, "Alignment of gold nanorods in polymer composites and on polymer surfaces," *Advanced Materials*, vol. 17, pp. 2173-2177, 2005.

[40] A. J. Haes and R. P. Van Duyne, "A highly sensitive and selective surface-enhanced nanobiosensor,", 723 ed 2002, p. O3.1.1-O3.1.6.

[41] G. Lu, T. Z. Forbes, and A. J. Haes, "SERS detection of uranyl using functionalized gold nanostars promoted by nanoparticle shape and size," *Analyst*, vol. 141, pp. 5137-5143, 2016.

[42] I. Mejac, W. W. Bryan, T. R. Lee, and C. D. Tran, "Visualizing the size, shape, morphology, and localized surface plasmon resonance of individual gold nanoshells by near-infrared multispectral imaging microscopy," *Analytical Chemistry*, vol. 81, no. 16, pp. 6687-6694, 2009.

[43] Z. Rosenzwlg and R. Kopelman, "Analytical properties and sensor size effects of a micrometer-sized optical fiber glucose biosensor," *Analytical Chemistry*, vol. 68, pp. 1408-1413, 1996.

[44] S. Richard, "Second-harmonic generation in tapered optical fibers," *J. Opt. Soc. Am. B*, vol. 27, no. 8, pp. 1504-1512, 2010.

[45] Z. Liu, C. Guo, J. Yaug, and L. Yuan, "Tapered fiber optical tweezers for microscopic particle trapping: fabrication and application," *Optics Express*, vol. 14, no. 25, pp. 12510-12516, 2006.

[46] S. Mondal, S. Pal, D. Kumbhakar, U. Tiwari, and R. Bhatnagar, "Evanescent wave assisted nanomaterial coating," *Applied Optics*, vol. 52, no. 22, pp. 5455-5459, 2013.

[47] X. Zhang, W. Peng, and Y. Zhang, "Fiber fabry-perot interferometer with controllable temperature sensitivity," *Optics Lett.*, vol. 40, no. 23, pp. 5658-5661, 2015.

[48] H. Heinzelmann and D. Pohl, "Scanning near-field optical microscopy," *Applied Physics A*, vol. 59, pp. 89-101, 1994.

[49] B. Puygranie and P. Dawson, "Chemical etching of optical fibre tips experiment and model," *Ultramicroscopy*, vol. 85, pp. 235-248, 2000.

[50] P. Lambelet, A. Sayah, M. Pfeffer, C. Philipona, and F. Weible, "Chemically etched fiber tips for near-field optical microscopy: a process for smoother tips," *Applied Optics*, vol. 37, no. 31, pp. 7289-7292, 2015.

[51] A. Lazarev, N. Fang, Q. Luo, and X. Zhang, "Formation of fine near-field scanning optical microscopy tips. Part I. By static and dynamic chemical etching," *Review of Scientific Instruments*, vol. 74, no. 8, pp. 3679-3683, 2003.

[52] P. Hoffman, B. Dutoit, and R.-P. Salathe, "Comparison of mechanically drawn and protection layer chemically etched optical fiber tips," *Ultramicroscopy*, vol. 61, pp. 165-170, 1995.

[53] S. S. Pal, S. K. Mondal, U. Tiwari, V. G. Swamy, M. Kumar, N. Singh, P. P. Bajpai, and P. Kapur, "Etched multimode microfiber knot-type loop interferometer refractive index sensor," *Review of Scientific Instruments*, vol. 82, pp. 095107-1-095107-4, 2011.

[54] A. Urban, S. Carretero-Palacios, A. Lutich, T. Lohmuller, J. Feldmann, and F. Jackel, "Optical trapping and manipulation of plasmonic nanoparticles: fundamentals, applications, and perspectives," *Nanoscale*, no. 6, pp. 4458-4474, 2014.

[55] A. Ashkin, "Optical trapping and manipulation of neutral particles using lasers," *Proceedings of the National Academy of Sciences*, vol. 94, pp. 4853-4860, 1997.

[56] K. C. Neuman and S. M. Block, "Optical Trapping," *Review of Scientific Instruments*, vol. 75, no. 9, pp. 2787-2809, 2004.

[57] K. Sasaki, M. Koshioka, H. Misawa, N. Kitamura, and H. Masuhara, "Optical trapping of a metal particle and a water droplet by a scanning laser beam," *Applied Physics Letters*, vol. 60, no. 7, pp. 807-809, 1992.

[58] K. Svoboda and S. M. Block, "Optical trapping of metallic Rayleigh particles," *Optics Letters*, vol. 19, no. 13, pp. 930-932, 1994.

[59] J. O. Trevisanutto, A. Linhananta, and G. Das, "Plasmonic structure: fiber grating formed by gold nanorods on a tapered fiber," *Optics Lett.*, vol. 41, no. 24, pp. 5789-5792, 2016.

[60] D. Vobornik and S. Vobornik, "Scanning near-field optical mircoscopy," *Bosnian journal of basic medical sciences*, vol. 8, no. 1, pp. 63-71, 2008.

[61] S. Link, Z. L. Wang, and M. A. El-Sayed, "How does a gold nanorod melt?," *Journal of Physical Chemistry B*, vol. 104, no. 33, pp. 7867-7870, 2000.

[62] B. Sharma, R. R. Frontiera, A.-I. Henry, E. Ringe, and R. P. Van Duyne, "SERS: materials, applications, and the future," *Materials Today*, vol. 15, no. 1-2, pp. 16-25, 2012.

[63] M. Suzuki, Y. Niidome, Y. Kuwahara, N. Terasaki, K. Inoue, and S. Yamada, "Surface-enhanced nonresonance Raman scattering from size- and morphology-controlled gold nanoparticle films," *Journal of Physical Chemistry B*, vol. 108, no. 31, pp. 11660-11665, 2004.

[64] S. D. Roy, M. Ghosh, and J. Chowdhury, "How hottest geometries and adsorptive parameters influence the SER(R)S spectra of methylene blue molecules adsorbed on nanocolloidal gold particles of varied sizes?," *Spectrochimica Acta Part A-Molecular and Biomolecular Spectroscopy*, vol. 151, pp. 796-806, 2015.

[65] Y. Bai, L. Yan, J. Wang, L. Su, N. Chen, and Z. Tan, "Highly reproducible and uniform SERS substrates based on Ag nanoparticles with optimized size and gap," *Photonics and Nanostructures - Fundamentals and Applications*, vol. 23, pp. 58-63, 2017.

[66] M. Y. Tsvetkov, B. N. Khlebtsov, V. A. Khanadeev, V. N. Bagratashvili, P. S. Timashev, M. Samoylovich, and N. G. Khlebtsov, "SERS substrates formed by gold nanorods deposited on colloidal silica films," *Nanoscale Research Letters*, vol. 8, no. 250, pp. 1-9, 2013.

[67] G. Andrade, M. Fan, and A. G. Brolo, "Multilayer silver nanoparticles-modified optical fiber tip for high performance SERS remote sensing," *Biosensors and Bioelectronics*, vol. 25, pp. 2270-2275, 2010.

[68] A. M. Michaels, M. Nirmal, and L. E. Brus, "Surface enhanced Raman spectroscopy of individual rhodamine 6G molecules on large Ag nanocrystals," *Journal of the American Chemical Society*, vol. 121, no. 43, pp. 9932-9939, 1999.

[69] L. Jensen and G. C. Schatz, "Resonance Raman scattering of rhodamine 6G as calculated using time-dependent density functional theory," *Journal of Physical Chemistry A*, vol. 110, no. 18, pp. 5973-5977, 2006.

[70] H. Watanabe, N. Hayazawa, Y. Inouye, and S. Kawata, "DFT vibrational calculations of rhodamine 6G adsorbed on sliver: analysis of tip-enhanced Raman spectroscopy," *Journal of Physical Chemistry B*, vol. 109, no. 11, pp. 5012-5020, 2005.

[71] P. MAtteini, M. Cottat, F. Tavanti, E. Panfilova, M. Scuderi, G. Nicotra, M. C. Menziani, N. Khlebtsov, and M. de Angelis, "Site-selective surface-enhanced Raman detection of proteins," *Acs Nano*, vol. 11, pp. 918-926, 2017.

[72] L.-J. Xu, C. Zong, X.-S. Zheng, P. Hu, J.-M. Feng, and B. Ren, "Label-free detection of native proteins by surface-enhanced Raman spectroscopy using iodide-modified nanoparticles," *Analytical Chemistry*, vol. 86, pp. 2238-2245, 2014.